Optimization of a Vortex-Induced Vibration-Based Energy Harvester by Lock-in Phenomenon

by Vishak Sivadas

B.E. in Mechanical Engineering, August 2009, University of Pune

A Thesis submitted to

The Faculty of
The School of Engineering and Applied Sciences
of The George Washington University
in partial fulfillment of the requirements
for the degree of
Master of Science

January 31, 2012

Thesis directed by

Adam M. Wickenheiser

Assistant Professor of Engineering and Applied Science

Dedication

To

My parents

Acknowledgments

First, I thank my advisor Dr. Adam M. Wickenheiser. His support and guidance is the main reason that this thesis is completed. I would like to thank everyone in the Mechanical and Aerospace Engineering department that I had the privilege to work with and learn from during my studies. I thank Dr. Chunlei Liang and Dr. Philippe M. Bardett for their insightful comments and suggestions for this research. I greatly appreciate the discussions and exchange of ideas with my friends and colleagues: Dr. Kartik Bulusu, Chris Blower, Matthieu Andre, Amy McCleney, Megan Grannan and Liam Cusack. Finally, I would like to say to all my family and friends, back home and abroad, that I am grateful for your support over the years.

Abstract

Optimization of a Vortex-induced Vibration-based Energy Harvester by Lock-in Phenomenon

This dissertation presents a study of small-scale, vortex-induced vibration-based wind energy harvesting structures consisting of a bluff-body with a piezoelectric-mounted cantilever beam. The purpose of these devices is to harness the significant wind energy existing in the boundary layers around naturally occurring and manmade structures. The rapid variation of pressure and velocity in the boundary layers around these structures can be tapped and used to power structural health monitoring systems or applied to border security sensors that consist of densely populated wireless sensor nodes, offering a reduction in the costs of battery replacement and wiring.

The proposed device is a miniature, scalable wind harvesting device. This energy harvesting device couples three different physical domains: fluid, structural and electrical. The configuration consists of a bluff-body with a flexible piezoelectric cantilever attached to the trailing edge. As the cantilever beam vibrates due to shed vortices from the bluff body, the strain energy in its deformation is converted into electrical energy by piezoelectric transduction.

This study employs the use of COMSOL multiphysics software using the fluid-structure interaction module for Computational Fluid Dynamics (CFD) modeling and simulations. The results from the CFD modeling are interfaced with MATLAB for further electromechanical simulations. A linearized dynamic mathematical electro-mechanical

model of a vibrating cantilever beam associated with energy harvesting is also presented. Simulations are run for different characteristic dimensions, shapes for the bluff body, length-to-diameter ratio, and optimized for maximum power over a wide range of flow velocities. The harvester is optimized by the phenomenon of lock-in. Lock-in is defined to occur when the cantilever oscillates at the same frequency as the undisturbed wake behind the bluff body. The integrated fluid-structure interaction with the piezoelectric module is used to find the different non-dimensionless parameters that are important to study the energy harvesting model for higher efficiencies.

The most optimized harvester design from this study, in terms of efficiency and range of lock-in bandwidth, is achieved by the D-shaped bluff body harvester, compared to cylindrical and pentagonal bluff bodies. The average total efficiency of the D-shaped bluff body between the lock-in bandwidth is found to be 0.0037.

Table of Contents

Acknowledgments ..... **iv**

Abstract ..... **v**

Table of Contents ..... **vii**

List of Figures. ..... **x**

List of Tables ..... **xiii**

List of Symbols ..... **xiv**

Glossary of Terms ..... **xviii**

Chapter 1: Introduction **1**

1.1 Thesis Problem 1

1.2 History of VIV- The Fundamental Basis 2

1.3 VIV-based Literature 3

1.3.1 Reduction of VIV Effect 5

1.3.2 Postive Effect of VIV 6

1.4 Piezoelectric Energy Harvesting from Flowing Media Literature R-

-eview 8

Chapter 2: FSI Basics and Parameters **11**

2.1 Dimensionless Parameters 11

2.1.1 Reynolds Number 17

2.1.2 Strouhal Number 18

2.1.3 Reduced Velocity 19

2.1.4 Lock-in 20

2.2 Fluid-Structure Interaction Basics.....21

2.2.1 Fluid Motion 21

2.2.2 Structural Motion.....22

2.2.3 Fluid-Structure Interaction Interface 23

Chapter 3: Derivation of the Electromechanical Modeling.....28

3.1 Derivation of Euler-Bernoulli Type Cantilever Beam.....28

3.2 Electromechanical Coupling Derivation.....31

Chapter 4: Simulation and Results 40

4.1 Problem Setup.....40

4.1.1 Geometry 40

4.1.1.1 Bluff Bodies Investigated.....40

4.1.1.2 Geometry Modeling.....40

4.1.1.3 Mesh Generation 41

4.1.2 Boundary Condition.....42

4.2 Simulation and Results.....45

4.2.1 Strouhal Number Analysis 45

4.2.2 Analysis of Different L/D Ratios of the Cantilever Beam...47

4.2.3 Transduction Efficiency of the Model.....51

Chapter 5: Conclusions and Future Work 82

5.1 Conclusions 82

5.2 Future Work 84

References 85

Appendix 89

List of Figures

Figure 1-1- von Kármán vortex streets forming in the wake of a bluff-body…….....……...13

Figure 1-2- A schematic of the Gerrard theory of vortex shedding, showing the vortex bein--g drawn across and cutting off the opposite vortex from the feeding sheet ……..14

Figure 1-3- Ferrybridge cooling tower collapse due to VIV……..…….....15

Figure 1-4- The destructive nature of VIV is best explained by the Tacoma Narrows Bridge Disaster in Tacoma, Washington, 1940…….....16

Figure 2-1- Movement of the cantilever beam due to the vortex force……..….....26

Figure 2-2- One-dimensional example of Lagrangian, Eulerian and ALE mesh and particle motion…….……....……...…27

Figure 3-1- Layout of a cantilever beam in bending…….....36

Figure 3-2- Layout and geometric parameters of cantilevered vibration energy harvester in parallel bimorph configuration…….……..…37

Figure 4-1- Bluff Bodies Investigated…….…..…....57

Figure 4-2- Representation of triangular mesh with D-Shaped as the bluff body and the cantilever beam……..…....58

Figure 4-3- Diagrammatic representation of boundary conditions used in the CFD Simulation……...……...59

Figure 4-4- Velocity and Vorticity contour plots for a cylindrical bluff-body (Re=1200) ……...60

Figure 4-5- Velocity and Vorticity contour plots for a Triangular bluff-body (Re=1200) ……..…….61

Figure 4-6- Velocity and Vorticity contour plots for a pentagonal bluff-body (Re=1200) ……..……...…….….62

Figure 4-7- Velocity and Vorticity contour plots for a D-shaped bluff-body (Re=1200)….……..…....63

Figure 4-8- Strouhal Number Vs Reynolds number for different bluff-body shapes.....64

Figure 4-9 Reynolds number Vs Frequencies of cantilever-alone and bluff body-alone for cylindrical bluff body...……...……...65

Figure 4-10- L/D ratio = 1.6..……...…….66

Figure 4-11- L/D ratio = 1.7……...…….67

Figure 4-12- L/D ratio = 1.8…….....…….……..68

Figure 4-13- Magnified version of L/D ratio = 1.6 …….……...69

Figure 4-14- Magnified version of L/D ratio = 1.7 ……..……...70

Figure 4-15- Magnified version of L/D ratio = 1.8 ……..……...71

Figure 4-16- D-shaped locked-in Re=195, L/D=1.7 ……...72

Figure 4-17- D-shaped de-synchronized Re=250, L/D=1.7 ……....….72

Figure 4-18- Cylinder locked-in Re=181, L/D=1.7…….....73

Figure 4-19- Cylinder de-synchronized Re=240, L/D=1.7……..……73

Figure 4-20- Pentagon locked-in Re=180, L/D ratio = 1.7……..…74

Figure 4-21- Pentagon de-synchronized Re=200, L/D ratio = 1.7……...…74

Figure 4-22- Cylinder with different L/D ratios, Re=18……..76

Figure 4-23- Energy efficiency of a cylindrical bluff-body model Re=121……...…..77

Figure 4-24- Energy efficiency of a cylindrical bluff-body model Re=180……...…..78

Figure 4-25- Energy efficiency of a D-shaped bluff-body model Re=180……..…78

Figure 4-26- Energy efficiency of a D-shaped bluff-body model Re=200……..…78

Figure 4-27- Energy efficiency of a pentagonal bluff-body model Re=180……....79

Figure 4-28- Energy efficiency of a pentagonal bluff-body model Re=200……..…..79

List of Tables

Table 1 Geometry and material properties……...37

Table 2 Calculated Values for Harvester Parameters……...38

Table 3 Fluid property varying parameters……..54

Table 4 Fluid property range and values……..55

Table 5 Average electric power for different bluff-bodies……...80

Table 6 Average power efficiencies for different bluff-bodies at L/D ratio =1.7……81

List of Symbols

A	Area of the bluff body
b	Width of the bluff body
D	Characteristic dimension of the bluff body
U	Free stream velocity
ν	Kinematic viscosity
μ	Dynamic viscosity
U^*	Reduced velocity
u, v ,w	Velocity in the x, y and z direction
f_s	Frequency of vortex shedding
f_n	Natural frequency of the cantilever beam
P_{mech}	Mechanical power
P_{elec}	Electric power

L	Length of the cantilever beam
T	Thickness of the cantilever beam
n	Outward normal to the boundary
I	Identity matrix
f	Reaction force on the fluid
p	Pressure
ρ	Density
w	Transverse displacement
$(\rho A)_{eff}$	Mass/ unit length
V	Shear force
M	Bending moment
$(EI)_{eff}$	Flexural rigidity
T	Stress

S	Strain
E	Electric field
D	Electric displacement
c	Young's modulus
e	Piezoelectric constant
ε	Dielectric constant
q	Charge
i	Current
k	Material coupling coefficient
θ	Piezoelectric patch coupling coefficient
C_0	Capacitance
R_L	Impedance
t	time

$(.)^{E}$ Linearization at constant electric field

$(.)^{S}$ Linearization at constant strain

Glossary of Terms

ALE	Arbitrary Eulerian Lagrangian
FSI	Fluid-structure interaction
Re	Reynolds number
St	Strouhal number
VIV	Vortex induced vibration
CFD	Computational fluid dynamics
1-D	One dimensional
2-D	Two dimensional
3-D	Three dimensional
VIVACE	Vortex Induced Vibration for Aquatic Clean Energy
PZT	Piezoelectric transducer

Chapter 1: Introduction

Energy harvesting is the process of capturing minute amounts of energy from one or more naturally-occurring energy sources - for example thermal, solar, wind or mechanical energy - accumulating it, and storing it for later use. In recent years, an increasing amount of research has been done on generating vibration-based energy by fluid-structure interaction through piezoelectric transducers. Whenever a stationary bluff object is immersed in a flowing medium, driving oscillating forces are generated on either end of the bluff-body. These oscillating forces can mechanically strain piezoelectric cantilever beams attached to the bluff-body and produce electricity useful for powering wireless devices, for example.

1.1 Thesis Problem

The essential goal of this thesis is to create a new optimized design for a small-scale wind energy harvesting using bluff-body and Vortex Induced Vibration (VIV) phenomena in order to investigate the power generated for a wide range of flow speeds. If the piezoelectric cantilever beam resonates at a frequency equivalent to the vortex shedding frequency, maximum energy can be extracted. The beam reaches maximum amplitude at resonance but it does not mean that increasing flow speed cannot increase the power even if the beam is not in resonance. In order to test this hypothesis, both these phenomena are investigated by attaching a flexible piezoelectric cantilever at the trailing edge of a bluff-body, and the effect of nonlinear vibrations of the cantilever beam at a wide range of velocities is thoroughly studied. The Computational Fluid Dynamics (CFD) aspect of the

fluid-structure interaction problem is investigated by using the commercial software COMSOL Multiphysics. The fluid-structure interaction module in COMSOL Multiphysics consists of the Navier-Stokes equation used in the fluid domain, linear elastic modeling equations in the solid domain, and an integration of these two domains through a moving mesh capability. An explanation of these physics domains are given in chapter 2 of the thesis study. The cantilever beam attached to the bluff-body model is required to function at a wide range of wind velocities in ambient conditions due to the unpredictable nature of wind. This functionality is examined by predicting the lock-in bandwidth, where the vortex shedding frequency locks into the natural frequency of the cantilever beam. The prediction of lock-in is investigated to find out the range of velocities where maximum strain energy can be extracted from the vibrations of the flexible cantilever beam to convert into electrical energy through piezoelectric transduction.

1.2 History of VIV- The Fundamental Basis

Flow-induced vibrations are the structural and mechanical oscillations of bodies immersed in or conveying fluid flow as a result of an interaction between the fluid-dynamic forces and the inertia, damping, and elastic forces in the structures. There has been documentation of this phenomenon beginning with the rabbinic records from thousands of years ago, when King David hung a stringed instrument over his bed at night and the wind would cause the strings to sound [1,2].

Bluff-bodies usually shed vortices in a subsonic flow. Coherent vortex streets are found at very small Reynolds number flows (Re<300), which is the primary regime of focus in this study. The earliest literature on Vortex-Induced Vibration (VIV) was written when Leonardo da Vinci first observed wind-induced vibrations in 1504 AD in the form of "Aeolian Tones" from the taut wires of an Aeolian harp. The first systematic investigation of vortex-induced oscillations was completed in 1878 by Strouhal [3,4], whose experiment consisted of spinning a stretched wire or rod about an axis parallel to its length, thus creating a uniform lengthwise cross flow. In fact, he believed that the stretched wire oscillated parallel to the wind and that the oscillations were induced by a friction-like force akin to the action of a bow on a violin string. These conceptions were doubted by Rayleigh, who observed experimentally in 1879 that the wire actually vibrates perpendicular to the wind and later correctly identified the source of vibration as the instability of vortex streets [5].

Afterwards, in the 20th century the deadly collapse of the Tacoma Narrows Bridge reinvigorated research in the area of VIV, covering a broad range of aspects in this field. Blevins' book on the subject covers many facets of the phenomenon of flow-induced vibrations and is referenced extensively throughout this project; the reader may find it very useful as an introduction to the topic [1].

1.3 VIV- based Literature

A simple explanation of VIV is put forward in this section in order to familiarize the reader with this phenomenon. For a cylinder when Reynolds number (ratio of inertia force and viscous force of the fluid) is greater than 40, vortex shedding occurs. The vortices shed with opposite direction of rotation from opposite sides of the cylinder (see figure 1-1). This is because flow separation occurs and the shear layer rolls up into a vortex. The only stable arrangement is for the vortices to alternate as was shown mathematically by von Kármán, making one larger than the other at all times. The actual mechanism of vortex shedding is not known for certain. However, a generally accepted theory is that the larger vortex draws the smaller vortex across the wake causing the shear layers to interact, which effectively cuts off the supply to the larger vortex, forming a vortex pair; this vortex is then shed and carried downstream. The smaller vortex is now the larger one and the process continues, as represented in Figure 1-2. This theory was first developed because it was found when a splitter plate was placed on the downstream side of the cylinder, the vortices remained attached to the cylinder, supposedly because they did not interact as described. This is also shown in Figure 1-2. Vortex shedding leads to periodic variations in the lift and drag forces. The lift force has a period equal to the vortex shedding frequency. When a degree of freedom is allowed in the cross-flow direction, these variations in the lift force induce vibrations, or VIV. As part of the above explanation, the mechanism of vortex formation can be simply stated as-

"When a flowing fluid is unable to negotiate its way smoothly around a bluff object, the phenomenon of periodic vortex shedding occurs" [3].

1.3.1 Reduction of VIV effect

A vast amount of work has been done in the area of vortex-induced vibrations, covering a broad range of aspects. Hall studied this VIV phenomenon using a semi-empirical modeling approach that includes extensive study of harmonically forced cylinders, spring-mounted cylinders, and taut elastic cables. His dynamic model is a coupled fluid and structural oscillator. The vortex shedding from the fluid oscillator equation creates fluctuating lift force on the structure. The motion of the structural oscillator provides a synchronous tripping mechanism for vortex shedding, causing lock-in. Although his idea was to reduce the vortex-induced vibrations of the above mentioned models, the dimensionless numbers and analytic approach he developed was important for our study in terms of the modeling and simulation approach. In this study, the approach is to strain the cantilever beam through fluid passing over stationary bluff-bodies. The drawback of his model is that the empirical parameters had to be matched for each experiment. This study in comparison with Hall's study uses a coupling of fluid structural coupling through Arbitrary Eulerian-Lagrangian method. Hall's modeling approach is simpler than the present modeling approach in that a finite element method is used to model the "Aero-electro-mechanical" coupling. Sarpkaya and Blevins studied vortex-induced oscillations in a few specific fundamental cases such as vortex shedding from a stationary bluff body;

furthermore, they investigated the consequences of the lock-in phenomena, added mass, damping, and dynamic response measurements [1, 3, 5]. Dynamic response measurements help us understand the change in the motion of the beam to changes in a fluid flow. The displacement amplitude, frequency response etc. help us in defining whether the system changes with respect to fluid flow changes. Bearmen dealt with vortex shedding from externally forced oscillating bodies [6].

A thorough review was provided by Williamson and Govardhan [7], covering the entire field, the work that has been done, and questions that still remain. In that paper, they were concerned principally with the oscillations of an elastically mounted rigid cylinder; with forced vibrations of such structures; with bodies in two degrees of freedom; and with dynamics of cantilevers, pivoted cylinders, cables and tethered bodies [7]. Most of these studies are confined to the flowing medium water. The density of air being smaller compared to water, this study deals with low Reynolds number in the order of 10-1000. Water, having higher density compared to air, has a significant effect on the added mass ratio. The section below explains how the positive effect of VIV is used and transferred to different applications.

1.3.2 Positive effect of VIV

VIV occurs in many engineering situations, such as bridges, stacks, transmission lines, aircraft control surfaces, offshore structures, marine cables, pipelines etc., and many of the

researchers have tried to reduce the effects of VIV on all these above mentioned engineering situations. An example of which is mounting helical strakes on the pipes being used for deep-water risers in the offshore oil and gas industries. A group of researchers led by Bernistas from University of Illinois, Urbana Champagne invented a new technology which consisted of cylinders extracting energy from underwater current. Unlike other researchers, this team used the positive effects of VIV to extract energy from the environment. This interesting technology is named as VIVACE (Vortex Induced Vibration for Aquatic Clean Energy) [8]. It consists of a rigid circular cylinder mounted on elastic springs and connected to a Power Take-off (PTO) system via a transmission mechanism. The cylinders are on the order of 1m long and 0.1m in diameter and are coupled to a generator. The body undergoes vortex-induced vibrations and, through a transmission system, transmits the mechanical energy to a generator for conversion to electricity or directly to a mechanical or hydraulic form of usable energy. The resulting mechanical energy is transmitted via a gear-belt system to a generator and converted to electricity. The cost per kWh of VIVACE is really low (0.055$/kWh) compared to wind turbine, solar energy and other alternate energy resources, but VIVACE works only using underwater currents and not air as a medium. Also it is categorized into higher energy density alternate energy resources with wind energy, solar energy, energy from landfill gas etc. The cost per kWh of VIVACE is 0.025-0.065$/kWh less than conventional hydroelectric power

generation (electrical power through the use of the gravitational force of falling or flowing water on turbines).

Unlike VIVACE, this study concerns a small-scale wind energy harvesting system. The power harnessed from this study is within the range of energy densities similar to sensor-like devices. VIVACE gave this study an idea about how to optimize the whole system using dimensionless parameters. Williamson, Bearman, Blevins etc. gave this thesis study an insight into how to build the best possible design using different parameters and concepts regarding VIV and bluff-body vibrations. One of the main contributions to the engineering field in the present study is the physical modeling, simulation and investigation of different flow physics over stationary bluff bodies and finding the synchronous region when the stationary bluff body is attached to the cantilever beam model. Another novel idea used in this study is the use of air as the flowing medium. Only Feng and Parkinson [9] studied VIV using air as a medium, but his device did not have a stationary bluff-body or a cantilever beam attached to it. He investigated a moving oscillating cylinder and D-section cylinder, including detailed measurements of frequencies, displacement amplitudes, phase shift of the exciting force with respect to the displacement, and spanwise correlation of wake velocities and fluctuating surface pressures on oscillating cylinders.

1.4 Piezoelectric Energy Harvesting from Flowing Media Literature Review

Vortex-induced vibrations (VIV), bluff body vibrations, aeroelastic fluttering [10] and wake galloping phenomena [11] have been extensively investigated by researchers for small-scale piezoelectric wind harvesting [12]. For example, the driving oscillating forces that mechanically strain the piezoelectric cantilevers can be generated in a flowing medium (air or water) by either an obstacle in the flow such as a bluff body or a so called "von Kármán vortex street". An external flapping mechanism was put forward by a group from Princeton University that investigated the feasibility of placing a piezoelectric membrane or "eel" in the wake of a bluff body. The main aim was to maximize the strain energy and mechanical power by coupling the unsteady hydrodynamic flow field with the vibrations of the membrane [13]. Two different designs were investigated by Pobering et al [14, 15]. The first harvester consists of nine, three-dimensionally arranged bimorph piezoelectric cantilevers. Each single cantilever consists of two layers of piezoelectric material (PZT) with three surface electrodes on top, on bottom and between the layers. Power values of up to 0.1 mW and output voltages of 0.8 V have been achieved with a non-optimized geometry. The second model was optimized using the results obtained with the previous model. A total of 18 piezoelectric cantilevers have been arranged in two rows upon each other. The energy harvester was able to supply 2 mW of power at a wind velocity of 8 m/s from the second mode [14]. Akaydin et al have investigated a VIV-based energy harvester with short-length piezoelectric beams kept in the wake of the cylinder with water as the

flowing medium [16]. The maximum power output, i.e. the maximum strain in the material, is measured when the tip of the beam is about two diameters downstream of the cylinder. The combination of two mechanisms contributed to this outcome. The first mechanism is the impingement of induced flow by the passing vortices on one side of the beam, and the second is the low pressure core region of the vortices that is present at the opposite side of the beam. The driving mechanisms mentioned above are mainly due to the passage of vortices formed by the shear layers emanating from the cylinder over the piezoelectric beam. They have also studied the power efficiency of the fluid power to the structural power. Compared to this study, they did not have a fixed theoretical explanation of the conversion of fluid power to structural power. The study helped this thesis in determining the dimensions of the geometry and scalability of the model for predicting the length of the cantilever beam.

A study using air as the flowing medium has been investigated by Li et al [17], who put forward a conceptual design describing a parallelized flapping piezo-leaf generator. The design had a vertical-stalk type piezoelectric harvester and exhibited improved output power density compared to the horizontal-stalk leaf design. The phenomenon of fluttering was proposed by Bryant et al. and Li et al [17, 18]. A simple two-degree-of-freedom aeroelastic power harvester is put forward by Bryant et al [18]. The energy harvester consists of a rigid flap connected by a ball bearing revolute joint to the tip of a flexible beam. They concluded that the energy harvester has a minimum cut-in speed below which

it cannot operate. They found that, in a varying flow application, the energy harvesting system would need to be tailored to have a cut-in wind speed low enough for the device to operate throughout the expected flow speed range and the bender and system resonance peaks placed to maximize power output throughout the range of expected flow speeds. The Princeton University group used the VIV mechanism and also the flowing medium as water unlike Bryant et al. and Li et al. who used the principle of fluttering.

In order to maximize harvested power, vibration-based generators are designed to match one of their natural frequencies – typically the fundamental frequency – to the base excitation frequency [19]. Vortex shedding frequencies in the wake due to fluid flow over a bluff body depend on the Reynolds number, Strouhal number [20, 21], smoothness of the structure, [22- 24] dimensions of the bluff body, and other factors [1]. Generally lock-in is defined to occur when the flexible structure oscillates at the same frequency as the undisturbed wake behind the bluff-body, but if the flow speed changes slightly, the vortex-shedding frequency remains locked into the resonant frequency and is defined to be synchronized.

When the flexible structure reaches this condition, its wavelength and amplitude are also similar to the undisturbed vortex street. An efficient VIV-based power generator should have a very wideband lock-in region since flow speed cannot be expected to remain constant.

The next few chapters explain the physical and mathematical modeling and simulation development of the thesis study. Chapter 2 gives the readers insight into the dimensionless parameters being used, the basic phenomenon of lock-in, and the mathematical and physical explanation behind the fluid-structure interaction modeling. The next chapter explains the electromechanical modeling, discussing the mathematical derivation of the structural Euler-Bernoulli beam theory and the linearized piezoelectric modeling required for calculating the electrical power generated. The final chapter includes the simulations, results and discussions pertaining to the study. This also includes the CFD simulations of the integrated fluid-structure interaction module and the MATLAB simulation results of the electromechanical modeling. The conclusion, future work and appendix follow afterwards. The appendix contains MATLAB codes for calculating electric power, mechanical power, frequency of vortex shedding, and Strouhal number.

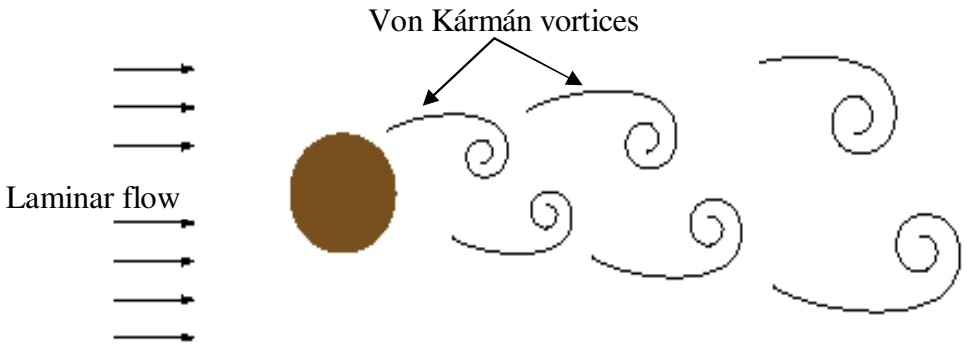

Figure 1-1- von Kármán vortex streets forming in the wake of a bluff-body

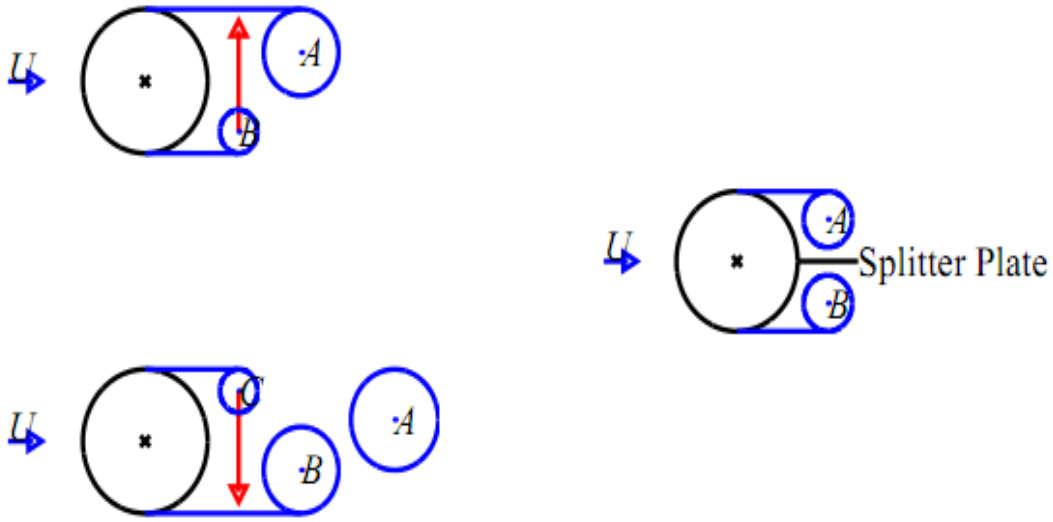

Figure 1-2- A schematic of the Gerrard theory of vortex shedding, showing the vortex being drawn across and cutting off the opposite vortex from the feeding sheet [25]

Figure 1-3- Ferrybridge cooling tower collapse due to VIV

Figure 1-4- The destructive nature of VIV is best explained by the Tacoma Narrows Bridge Disaster in Tacoma, Washington, 1940

Chapter 2: FSI Basics and Parameters

2.1 Dimensionless Parameters

The vibration of the cantilever attached to the bluff-body is described in terms of nondimensional parameters governing the fluid flow, the energy harvesting model, and the fluid-structure interaction. These parameters are useful for scaling flow-induced vibration and estimating the importance of different fluid phenomena. This chapter describes the different dimensionless numbers, the basic mechanism of lock-in, the physics behind fluid and structural domains, and the Arbitrary Eulerian-Lagrangian interface.

2.1.1 Reynolds Number

The Reynolds number, abbreviated Re, scales the boundary layer thickness and transition from laminar to turbulent flow. The boundary layer is impelled about the bluff-body by the inertia of the flow. Viscous friction at the model surface retards the boundary layer. By definition, the ratio of inertial force to viscous force in the boundary layer is

$$\mathrm{Re} = \frac{UD}{\nu} \tag{2.1}$$

where U, D and ν are the free stream velocity, characteristic dimension of the bluff-body, and kinematic viscosity of the fluid, respectively. The main significance of Re number is that it is used to predict the nature of vortex shedding at various flow speeds. At Re<5, for

a cylindrical bluff body, there is no flow separation. At higher Re<40, a fixed pair of vortices are seen in the wake of the bluff body. Until Re=150, a laminar vortex street regime is seen and at Re<300, the vortex streets flows into a transition range of turbulence.

2.1.2 Strouhal Number

The Strouhal number (S) is the dimensionless proportionality constant between the predominant frequency of vortex shedding and the free stream velocity divided by the bluff-body dimension. The Strouhal number (also called the Strouhal frequency) applies to only stationary bodies. This is a fundamental dimensionless number to VIV study. The Strouhal number is often approximated by a constant value. Lock-in will tend to change the value of Strouhal number: the frequency of vortex shedding becomes constant at lock-in and the free-stream velocity changes the value of the Strouhal number. For example, the Strouhal number for cylindrical bluff-bodies, for a wide range of Reynolds number, is approximated as St =0.21 in most of the literature.

$$St = \frac{f_s D}{U} \tag{2.2}$$

where, f_s is the frequency of vortex shedding.

This nondimensional number is thoroughly investigated for different bluff-body shapes in the simulation section of this thesis.

2.1.3 Reduced Velocity

The reduced velocity has sometimes been referred to as the velocity ratio, as it is a non-dimensional quantity. In the past when it was believed that only one vortex shed from each side during each cycle of motion of the body, the Strouhal Frequency was used to normalize the free-stream velocity. However, the most recent and more proper trend in VIV data analysis has been to use the natural frequency of the system instead. This parameter is often used as the independent variable on many plots since it properly collapses many test cases onto the same plot. The reduced velocity dimensionless quantity has the natural frequency of the beam in its definition, which is a constant. Also, all simulations are on the basis of different velocity range, hence it is much better to use than many other dimensionless quantities.

$$U^* = \frac{U}{f_n D} \tag{2.3}$$

where, f_n is the first (i.e. fundamental) natural frequency of the cantilever beam. This term in most previous studies is the natural frequency of the moving bluff-body. However, as this model has a stationary bluff-body and the vortices from the flow over the bluff-body act on the cantilever beam, the natural frequency is taken as the fundamental frequency of the beam.

2.1.4 Lock-in

A unique and key feature studied in this thesis is the frequency lock-in effect. This corresponds to the vortex shedding frequency locking into the frequency of vibrations of the cantilever beam, where the cantilever is also responding at the natural frequency. This is defined to occur when the cantilever beam oscillates or vibrates at the same frequency as the undisturbed wake behind the bluff-body. When the cantilever beam reaches this condition, its wavelength and amplitude are also similar to the undisturbed vortex streets. A simple mechanism of lock-in is explained: as the frequency of the unstable system (the wake) approaches that of the cantilever beam, the oscillating lift forces cause an increasing amplitude of motion by a standard resonance effect. Then, provided this amplitude is large enough, the wake is entrained to move at the natural resonating frequency of the cantilever beam. This feedback mechanism is implicitly assumed to be nonlinear, as the existence of lock-in and its extent depend on the amplitude of motion. So, when there is an effect of large amplitude in the lock-in region, the strain of the piezoelectric cantilever beam can be converted into appreciable power.

Lock-in occurs approximately when

$$f_s = f_n \text{ or } \frac{f_s}{f_n} = 1 \tag{2.4}$$

The frequency of vortex shedding may not always be equal to the natural frequency, but the frequency of response of the cantilever beam and the frequency response of vortex shedding will be approximately equal within the range of lock-in.

2.2 Fluid-Structure Interaction Basics

2.2.1 Fluid motion

Assuming the fluid to be incompressible and Newtonian, the fluid motion is governed by the incompressible Navier-Stokes equations:

$$\nabla \bullet \mathbf{u} = 0 \tag{2.5}$$

$$\rho_f \left(\frac{\partial \mathbf{u}}{\partial t} + \mathbf{u} \bullet \nabla \mathbf{u} \right) = -\nabla p + \mu \nabla \bullet \nabla \mathbf{u} \tag{2.6}$$

where $\mathbf{u}$ is the fluid velocity vector, p the pressure, ρ_f the density, and μ the dynamic viscosity. Solutions of Eqs. 2.5 and 2.6 yield the velocity and pressure fields. For a long cantilever vibrating at small amplitude, the flow field can be assumed to be two-dimensional. The 2-D Navier-Stokes equations in Cartesian coordinates are then

$$\frac{\partial v}{\partial x} + \frac{\partial w}{\partial z} = 0 \tag{2.7}$$

$$\rho_f\left(\frac{\partial v}{\partial t}+v\frac{\partial v}{\partial x}+w\frac{\partial v}{\partial z}\right)=-\frac{\partial p}{\partial x}+\mu\left(\frac{\partial^2 v}{\partial x^2}+\frac{\partial^2 v}{\partial z^2}\right) \tag{2.8}$$

$$\rho_f\left(\frac{\partial w}{\partial t}+v\frac{\partial w}{\partial x}+w\frac{\partial w}{\partial z}\right)=\frac{-\partial p}{\partial x}+\mu\left(\frac{\partial^2 w}{\partial x^2}+\frac{\partial^2 w}{\partial z^2}\right) \tag{2.9}$$

where v and w are the x and z velocity components, respectively. This set of equations yields the velocity and pressure fields, from which the fluid force exerted on the solid boundary can be calculated. This force is the negative of the reaction force on the fluid,

$$\mathbf{f}=-\mathbf{n}\cdot(p\mathbf{I}+\mu(\nabla\mathbf{u}+(\nabla\mathbf{u})^T)) \tag{2.10}$$

where $\mathbf{n}$ is the outward normal to the boundary and $\mathbf{I}$ is the identity matrix.

2.2.2 Structural motion

The solid mechanics interface in COMSOL describes the motion and deformation of solid objects. When the solid objects deform due to external or internal forces and constraints, each material particle keeps its material coordinates (uniquely defined by its position in some given initial or reference configuration), while its spatial coordinates

change with time and applied forces such that it follows a path in space. Because the material coordinates are constant, the current spatial position is uniquely determined by the displacement vector, pointing from the reference position to the current position. The present configuration assumes a linear elastic model. The total strain tensor is calculated from the displacement vector. This is coupled with the Euler-Bernoulli beam theory for cantilever beams described in the next chapter. The structural model assumes that only the normal component of the fluid stress affects the deformations of the solid bodies. The total strain tensor is written in terms of the displacement gradient:

$$S = \tfrac{1}{2}\left(\nabla \mathbf{w} + \nabla \mathbf{w}^{\mathbf{T}}\right) \tag{2.11}$$

where $\mathbf{w}$ is the displacement vector and S is the strain in the cantilever beam due to fluid pressure.

2.2.3 Fluid-structure interface

Fluid-Structure interaction (FSI) modeling is done with the help of COMSOL multiphysics interface, which combines fluid flow with solid mechanics to capture the interaction between the fluid and solid structure, as shown in Fig 2-1.

This interface uses an Arbitrary Lagrangian-Eulerian (ALE) method to combine the fluid flow formulated using an Eulerian description and a spatial frame with solid mechanics formulated using a Lagrangian description and a material (reference) frame. In structural mechanics, Lagrangian algorithms are used, where each node of the computational mesh coincides at each time with a material particle. This allows easy tracking of interfaces between different materials, but cannot handle larger displacements. On the contrary, fluid dynamical problems are solved using Eulerian algorithms, where the mesh is fixed and the material particle moves with respect to it. These algorithms allow easy treatment of large distortions, but cannot deal with interfaces and offer a poor resolution of flow details. ALE is the formulation of partial differential equations either in a spatial coordinate system, with coordinate axes fixed in space, or in a material coordinate system, fixed in the material in its reference configuration and following the material as it deforms [26]. A transformation of force is necessary as the Navier-Stokes equations are solved in the spatial (deformed) frame while the solid mechanics interfaces are defined in the material (un-deformed) frame. This is defined as

$$\mathbf{F} = \mathbf{f}\frac{dr}{dR} \tag{2.12}$$

where dr and dR are the mesh element scale factors for the spatial frame and the material (reference) frame, $\mathbf{F}$ is the transformation of force from the previous meshing frame, and $\mathbf{f}$

is the force on the fluid from Eq. (2.10). The coupling in the other direction consists of the structural velocities dw/dt (the rate of change for the displacement of the solid), which act as a moving wall for the fluid domain.

The numerical simulation of mechanical and/or fluid dynamical problems require the appropriate kinematic description of the considered continuum. The ALE algorithm combines the advantages and minimizes the drawbacks of the classical descriptions. Hence, a node of the mesh may move with the material particle following the Lagrangian description, held fixed as it is the case for Eulerian meshes, or even move in an arbitrary way to improve the quality of the mesh. Consequently, the ALE approach can handle greater displacements than the Lagrangian description and offers a higher resolution than the Eulerian method. Figure 2-2 shows an example of a one-dimensional Lagrangian, Eulerian and ALE mesh and particle motion. This example shows a comprehensive figurative description of a one-dimensional particle motion inside the cantilever beam due to fluid forces and the application of the Eulerian and Lagrangian meshing interface.

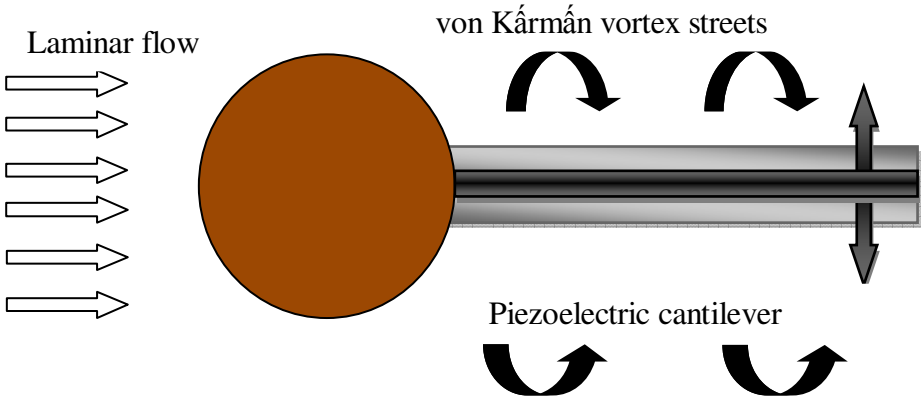

Figure 2-1- Movement of the cantilever beam due to the vortex force

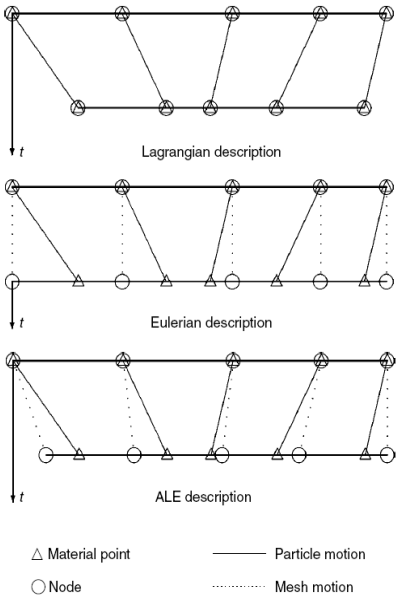

Figure 2-2- One-dimensional example of Lagrangian, Eulerian and ALE mesh and particle motion

Chapter 3: Derivation of the Electromechanical Modeling

A single-degree of freedom electromechanical model is employed in the proposed energy harvesting system. The cantilever beam is a flexible beam structure. Flexibility of structural components arises when the mass and stiffness properties are modeled as being distributed throughout the spatial definition of the component rather than at lumped positions. A distributed parameter system has infinite number of natural frequencies; however, the present model takes into account only the first mode of vibration. Hence it is a distributed parameter model reduced to a single degree of freedom model. The schematic diagram of the piezoelectric, vibration-based energy harvester considered in this study is presented in Figure 3-1. The assumptions used in formulating this model are that the beam is

- uniform along its span, or length, and slender
- composed of a linear, homogenous, isotropic elastic material
- such that rotary inertia and shear deformation can be neglected and only the normal component of pressure is associated
- considered to follow the linearized constitutive equations for modeling the piezoelectric effect, due to the fact that both mechanical and electrical perturbations are small and occur only in one direction

3.1 Derivation of Euler-Bernoulli Type Cantilever Beam

Consider the free-body diagram of an element of a beam shown in Fig. (3-1), where $M(x,t)$ is the bending moment, $V(x,t)$ is the shear force, and $p(x,t)$ is the external pressure (since it is 2D, this is force/length) difference between the upper and lower surfaces of the cantilever beam at each point x along the length of the beam and at each time t. The inertia force acting on the element of the beam is

$$(\rho A)_{eff}\, dx \frac{\partial^2 w(x,t)}{\partial t^2} \tag{2.11}$$

where x is the coordinate along the length of the beam, t the time, $w(x,t)$ the transverse displacement, and $(\rho A)_{eff}$ the mass per unit length.

The force equation of motion in the $z-$direction gives

$$-(V+dV)+p(x,t)dx+V=(\rho A)_{eff}\, dx \frac{\partial^2 w(x,t)}{\partial t^2} \tag{2.12}$$

The moment equation of motion about the $z-$axis is

$$(M+dM)-(V+dV)dx=p(x,t)dx\frac{dx}{2}-M=0 \tag{2.13}$$

By writing

$$dV = \frac{\partial V}{\partial x} dx \text{ and } dM = \frac{\partial M}{\partial x} dx \tag{2.14}$$

and disregarding terms involving second powers in dx, Eqs. 2.12 and 2.13 can be written as:

$$-\frac{\partial V(x,t)}{\partial x} + p(x,t) = \rho A(x) dx \frac{\partial^2 w(x,t)}{\partial t^2} \tag{2.15}$$

$$\frac{\partial M(x,t)}{\partial x} - V(x,t) = 0 \tag{2.16}$$

By using the relation $V = \frac{\partial M}{\partial x}$ from Eq. 2.16, Eq. 2.15 becomes

$$-\frac{\partial^2 M(x,t)}{\partial x^2} + p(x,t) = (\rho A)_{eff} \frac{\partial^2 w(x,t)}{\partial t^2} \tag{2.17}$$

From the elementary theory of bending of beams (Euler-Bernoulli or thin beam theory), the relationship between bending moment and deflection can be expressed as:

$$M(x,t) = (EI)_{eff} \frac{\partial^2 w(x,t)}{\partial x^2} \tag{2.18}$$

Inserting Eq. 2.18 into Eq. 2.17, we obtain the governing linearized dynamical equation of motion for the forced lateral vibration of a uniform beam:

$$(EI)_{eff} \frac{\partial^4 w(x,t)}{\partial x^4} + (\rho A)_{eff} \frac{\partial^2 w(x,t)}{\partial t^2} = p(x,t) \tag{2.19}$$

where x is the coordinate along the length of the beam, t the time, $w(x,t)$ the transverse displacement, $(EI)_{eff}$ the flexural rigidity, $(\rho A)_{eff}$ the mass per unit length, and $p(x,t)$ the pressure on the beam at each point x with respect to time.

3.2 Electromechanical Coupling Derivation

The harvester beam is excited due to the oscillating fluid pressure generated by the vortex forces. In the present configuration, a cantilever beam is placed at the wake of the bluff-body to study the transduction of fluid energy in the wake to mechanical energy. According to the schematic diagram, $w(x,t)$ (see Figure 3-3) is the relative deflection of the beam with respect to horizontal. This study assumes that the beam is vibrating near its fundamental natural frequency, and, consequently, the motion of the beam can be accurately described by one modal coordinate corresponding to the fundamental mode. Maximum energy is extracted when the first mode of vibration is excited. The higher-

frequency modes produce less strain compared to first natural frequency mode and can be assumed to be negligible if the vortex shedding frequency is not high enough to excite them.

The distributed-parameter dynamic equations of the cantilever beam are derived by force/moment balances. A cantilever beam with or without tip mass is the most widely used configuration for piezoelectric energy harvesting devices. The beam is assumed to be in pure bending; all other deformations are considered negligible. Piezoelectric material is bonded to both sides of the beam (bimorph configuration) to transform the vibrational strain energy into electrical signals.

Making the standard assumptions of Euler-Bernoulli beam theory from the previous chapter, a balance of forces and moments can be combined to yield

$$\frac{-\partial^2 M(x,t)}{\partial x^2} = (\rho A)_{eff} \frac{\partial^2 w(x,t)}{\partial t^2} - p(x,t) \tag{3.1}$$

Note that the base of the beam, i.e. the bluff-body, is fixed in all cases in this study. The linearized equations for the piezoelectric material are:

$$\begin{aligned} T_1 &= c_{11}^E S_1 - e_{31} E_3 \\ D_1 &= e_{31} S_1 + \varepsilon_{33}^S E_3 \end{aligned} \tag{3.2}$$

where T is stress, S is strain, E is electric field, D is electric displacement, c is Young's Modulus, e is piezoelectric constant, and ε is dielectric constant [27]. The subscripts indicate the direction of perturbation; in the cantilever configuration, 1 corresponds to x and 3 correspond to y (see Figure 3-2). The superscript $(.)^E$ indicates a linearization at constant electric field, and the superscript $(.)^S$ indicates a linearization at constant strain. Combining Eqs. 3.1 and 3.2, the following equation of motion of the beam is derived:

$$(\rho A)_{eff}\frac{\partial^2 w(x,t)}{\partial t^2}+(EI)_{eff}\frac{\partial^4 w(x,t)}{\partial x^4}+\theta\left[\frac{d\delta(x)}{dx}-\frac{d\delta(x-L)}{dx}\right]v(t)=p(x,t) \qquad (3.3)$$

where the effective beam parameters are listed in Table 1. The calculated values for the bimorph condition are given in Table 2. The electrical equation of motion is found to be [19]:

$$q(t)=\theta\left.\frac{\partial w(x,t)}{\partial x}\right|_{x=L}-C_0 v(t) \qquad (3.4)$$

The charge $q(t)$ in Eq. 3.4 is the sum of the strain coupling (proportional to the slope of the beam at the tip) and the charge displaced by the internal electric field. The electric current produced by the motion of the beam is thus

$$i(t) = \theta \left. \frac{\partial^2 w(x,t)}{\partial x \partial t} \right|_{x=L} - C_0 \frac{dv(t)}{dt} \tag{3.5}$$

The current term is replaced by the voltage and a constant resistance using Ohm's Law to calculate the voltage. The resistance is set by matching the impedance of the piezoelectric beam, $R_L = 1/(C_0 \omega_n)$. This impedance is indirectly evaluated from the frequency response of the beam. Inserting this resistance into Eq. 3.5 yields

$$\frac{v(t)}{R_L} = \theta \left. \frac{\partial^2 w(x,t)}{\partial x \partial t} \right|_{x=L} - C_0 \frac{dv(t)}{dt} \tag{3.6}$$

The internal piezoelectric capacitance is of order 10^{-8} (see Table 2), hence Eq. 3.6 can be reasonably reduced to:

$$v(t) = \theta R_L \left. \frac{\partial w^2(x,t)}{\partial x \partial t} \right|_{x=L} \tag{3.7}$$

Electric power is calculated from Eq. 3.7 using

$$P_{elec} = \frac{v^2(t)}{R_L} \tag{3.8}$$

The above derivation of the electromechanical model is integrated with the structural equation for Euler-Bernoulli cantilever beam theory and simulated through Matlab, the analysis of which is presented in the next chapter.

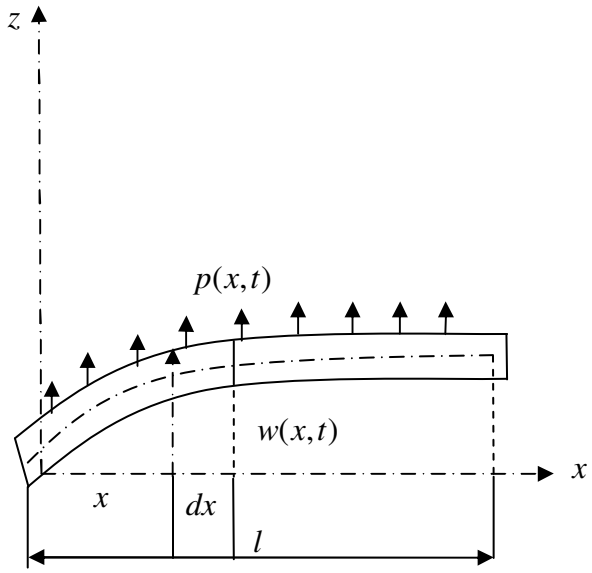

Figure 3-1-Layout of a cantilever beam in bending

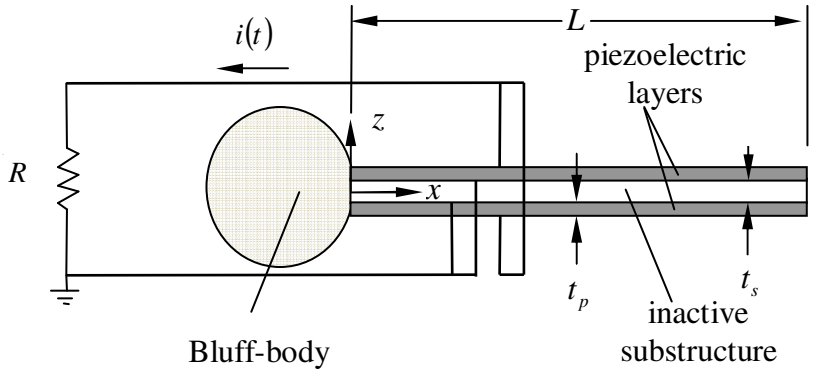

Figure 3-2- Layout and geometric parameters of cantilevered vibration energy harvester in parallel bimorph configuration [19]

Table 1-Geometry and material properties

Substrate material (mild steel)		
Young's modulus	c_s	210 GPA
Density	ρ_s	7850 kg/m^3
Piezoelectric material (PST-5A)		
Young's modulus	c_{11}^E	66 GPa
Density	ρ_p	7800 GPa
Piezoelectric constant	d_{31}	-190 pm/V
Permittivity	ε_{33}	15.93 nF/m
Material coupling coefficient	k_t^2	0.1496
Bimorph Energy harvester parameters		
Mass per unit length	$(\rho A)_{eff}$	$b_s\left(\rho_s t_s + 2\rho_p t_p\right)$
Effective stiffness	$(EI)_{eff}$	$c_s b_s \frac{t_s^3}{12} + 2c_{11}^E b_s\left[\frac{t_p^3}{12} + t_p\left(\frac{t_p + t_s}{2}\right)^2\right]$
Piezoelectric patch coupling coefficient	θ	$-e_{31} b_s\left(t_p + t_s\right)$
Capacitance	C_0	$\frac{2\varepsilon_{33}^S}{t_p} b_s L$

Table 2-Calculated Values for Harvester Parameters

Bimorph Energy harvester parameters		
Mass per unit length	$(\rho A)_{eff}$	0.2497 (kg/m)
Effective stiffness	$(EI)_{eff}$	1.8032 (Pa-m^4)
Piezoelectric patch coupling coefficient	θ	2.1318e- 04(C*m^2/N)
Capacitance	C_0	1.0620e-008 (F)

Chapter 4: Simulations and Results

This chapter describes the simulations and results involving the integrated fluid-structure interaction using COMSOL Multiphysics and the integrated structural-piezoelectric transduction simulations using Matlab. The first section details the step-by-step procedure to create the model of this system. The second section provides the analysis of the results obtained from the simulations.

4.1 Problem setup

4.1.1 Geometry

4.1.1.1 Bluff-bodies Investigated

The cylindrical bluff body is the most common bluff body shape investigated by researchers as part of VIV analysis. This wealth of historical data makes it easier for a lot of researchers, without investigating the complications of other bluff-body shapes for energy harvesting techniques. The four different bluff-body shapes investigated (see Figure 4-1) and the optimization of the energy harvester by figuring out the lock-in bandwidth is a novel idea which has never been explored by anyone on the basis of wind energy harvesting techniques.

4.1.1.2 Geometric modeling

The CAD tools in COMSOL Multiphysics provide many possibilities to create geometries using solid modeling. 1D, 2D and 3D geometric modeling can be done with the help of this CAD tool. During solid modeling, geometry is formed as a combination of solid objects using Boolean operations like union, intersection, and difference. These are called composite solid objects.

4.1.1.3 Mesh Generation

The next step in modeling the geometry for simulation is mesh generation. A mesh is a partition of the geometry model into small units of simple shapes. COMSOL Multiphysics software provides a mesh generator where 1D, 2D and 3D geometries can be meshed with ease.

This thesis is majorly concerned with 2D meshing techniques. For a 2D geometry, the mesh generator partitions the sub-domains into triangular or quadrilateral mesh elements. If the boundary is curved, these elements represent only an approximation of the original geometry. The sides of the triangles and quadrilaterals are called mesh edges, and their corners are mesh vertices. A mesh edge must not contain mesh vertices in its interior. Similarly, the boundaries defined in the geometry are partitioned (approximately) into mesh edges, so-called boundary elements, which must conform to the mesh elements of the adjacent sub-domains. If there are isolated points in the geometry, these also become mesh vertices. The geometry being investigated uses mainly a free mesh consisting of triangular elements. A quadrilateral mesh on geometry (mesh created by finite element method) is used when the geometry is stationary and the sub-domains are relatively regular in shape. For high-speed flows, the element growth rate also is increased due to the complicated fluid-structure interactions. The default element growth rate is initially set low, and if the simulation fails to converge, the element growth rate is increased. Element growth rate only applies to unstructured tetrahedral and triangle meshes. Figure 4-2 shows the meshing on the D-shaped bluff-body geometry.

4.1.2 Boundary Conditions

After meshing the geometry, the next step is to specify the boundary conditions for the closed system. This section explains the reason why certain flow conditions and boundary conditions are used for solving the transient fluid-structure interaction model (see Figure 4-3) and also the respective equations and approximations for the flow conditions.

(a) Inlet flow conditions

The inlet flow conditions taken into consideration in this study depend upon the Reynolds number value. The boundary condition for the inlet or the opening of the rectangular closed boundary system is the normal inflow velocity. The range of velocities used in this study is 0.01m/s to 3m/s. The equation for the inlet boundary condition is

$$\mathbf{u} = -\mathbf{n}U_0 \tag{4.1}$$

where $\mathbf{n}$ is the boundary normal pointing out of the domain and U_0 is the velocity magnitude in m/s.

(b) Walls

The wall feature represents wall boundaries in a fluid-flow simulation. On the longer sides of the rectangular boundary, the boundary condition at the wall has the with-slip

boundary condition. This is to approximate the fact that the boundaries are assumed to be farther apart in real world conditions and also to nullify any stress from the walls due to viscosity on the solid bluff-body-cantilever beam setup. The equations involved with the slip boundary condition are:

$$\mathbf{u} \bullet \mathbf{n} = 0 \tag{4.2}$$

$$[-\rho\mathbf{I} + \mu(\nabla\mathbf{u} + (\nabla\mathbf{u})^T)]\mathbf{n} = 0 \tag{4.3}$$

The slip conditions assume that there are no viscous effects at the slip wall and hence, no boundary layer develops. From a modeling point of view, this may be a reasonable approximation if the important effect of the wall is to prevent fluid from leaving the domain (which means that there is no flow across the boundary and no viscous stress in the tangential direction).

The boundary conditions applied on the solid bluff-bodies are with no-slip condition, which is given simply by

$$\mathbf{u} = 0 \tag{4.4}$$

Eq. 4.4 states that, for viscous fluids at solid boundaries, the fluid will have zero velocity relative to the boundary.

(c) Outlet

The outlet boundary conditions used are pressure with no viscous stress. This is used due to the fact that the flow is visualized to have a never ending outlet.

$$\mu(\nabla \mathbf{u} + (\nabla \mathbf{u})^T)]\mathbf{n} = 0 \tag{4.5}$$

This is apt for the study because it admits total control of the pressure level along the entire boundary.

(d) Linear elastic material model

This is the structural boundary condition for any solid interacting with the fluid incorporated by COMSOL Multiphysics. The linear elastic material model feature adds the equations for a linear elastic solid and an interface for defining the elastic material properties. The equations concerned with this boundary condition are the general strain tensor equation, the Hooke's law which relates the strain tensor with the stress tensor, and also the total force acting on the moving boundary, which is the body force and the stress force acting on the body due to fluid-structure interactions.

$$\rho \frac{\partial^2 w}{\partial t^2} - \nabla \bullet \sigma = \mathbf{F} \tag{4.5}$$

$$\mathrm{S} = \tfrac{1}{2}[(\nabla w)^T + \nabla w] \tag{4.6}$$

The linear elastic model also has a feature in which damping can be substituted for the solid boundary. The automatic isotropic damping feature is selected as the damping parameter due to the reason that the linear elastic solid boundary has the same properties in all directions.

Once the boundary conditions are set up, the next step is to simulate the transient model. The simulation results and approach on how the results are analyzed are described in the next section of this chapter.

4.2 Simulation and Results

This section is divided into different parametrical sections for the reader to have a clear idea of how the research work has been done. The first parametrical section concerns the Strouhal number for different bluff-bodies. The following section contains the dimensionless power and the analysis of efficiency of the system. Two types of energy conversions, fluid power to structural power and structural power to electric power, are investigated as part of the energy efficiency analysis. The fluid properties and varying fluid parameters used in the simulations are tabulated in Tables 3 and 4.

4.2.1 Strouhal Number Analysis

Strouhal numbers for different stationary bluff-body shapes are now presented. The frequency of vortex shedding is calculated by integrating the stress on the bluff-body in the z- direction from COMSOL simulations, thus giving the lift force. A Fast Fourier Transformation implemented in MATLAB is performed on the lift force yielding the frequency of vortex shedding. The oscillations in lift force (force perpendicular to the

flow) occur at the shedding frequency, whereas oscillations in the drag force (force parallel to the flow) occur at twice the shedding frequency. This is a consequence of the geometry of the vortex street [1]. The Strouhal number of a stationary bluff-body in a subsonic flow is a function of Reynolds number, and so this relationship is plotted herein. Earlier experimental studies have shown that most bluff-bodies have a Strouhal number around 0.2 for a wide range of Reynolds number. Our study confirms these results through CFD simulations, showing Strouhal numbers for different bluff-body shapes. This was the first step towards understanding the phenomenon of lock-in. According to the results obtained, the D-shaped bluff-body shows a constant Strouhal number value for the whole range of Reynolds numbers simulated. The physical significance of this statement is that the vortex shedding frequency of the D-shaped bluff-body scales linearly with the velocity for the Strouhal number constant over a wide range of velocities. Showing a similar trend with respect to the D-shaped bluff-body is the triangular bluff-body. Due to larger flow separation because of the evident geometry, the turbulence is higher than expected for lower Reynolds number flow regimes. COMSOL Multiphysics software has no option of simulating turbulence modeling under the fluid-structure interaction module. Hence, the triangular bluff-body could not be analyzed further as part of our modeling. The cylindrical bluff-body shows a constant Strouhal number for lower Reynolds number flows (Re=0-1500). The lift force of a cylindrical bluff-body is comparatively lower than that of the D-shaped bluff-body due to a reduced shear surface force and flow separation. Figures 4-4 through 4-7 show the CFD vorticity and velocity contour plots for different bluff-body sections. These show the formation of wake vortices for different bluff-body shapes. The contours for the vortices and velocities show the formation of vortex pairs. The vortex

formation is studied for a wide range of Reynolds number (Re=60-2000) for stationary bluff-bodies without the cantilever beam attached. These simulations were used mainly to calculate the frequency of vortex shedding by taking the inverse of the difference between the time periods for each vortex pair. The Strouhal number analysis helped this part of the thesis in tackling the question of which bluff-body shape to use in the next set of FSI simulations. Figure 4-8 shows how Strouhal number varies with respect to the Reynolds number. At low Reynolds number for all bluff bodies there is a constant linear increase in the Strouhal number due to a constant value for frequency of vortex shedding. This is the region where the cantilever beam resonates with the vortex shedding frequency. Hence, the lock-in occurs at this region. For increasing Reynolds number, Strouhal number becomes a constant due to a gradual increase in the vortex shedding frequency. Strouhal number is always approximated to a constant value (See chapter 2, section 2.1.2).

4.2.2 Analysis of different L/D ratios of the cantilever beam

The next set of simulations compare two different dimensionless numbers, ratio of vortex shedding frequency and natural frequency vs. reduced velocity, respectively. These ratios are computed to find out the lock-in bandwidth of different bluff-body models [28]. The geometry is divided into different categories of L/D (length of the cantilever to bluff-body dimension ratio) ratios. After initial simulations of L/D ratios ranging from 1.4 to 2.2, we came to the following conclusions:

- A smaller L/D ratio does not have higher power gain due to smaller piezoelectric patches mounted on the cantilever beam

- A larger L/D ratio tends to prevent vortex shedding over the beam, and hence the unsteady pressure is low amplitude

- The greatest lock-in bandwidth and greatest efficiency occurs at L/D=1.7

The mechanism behind the outcome of the results above is discussed in the next few paragraphs. Figure 4-9 shows the relation between the frequencies of cantilever-alone and bluff body-alone data for a cylindrical bluff body at L/D=1.7. The frequency from the bluff body converges to the frequency of cantilever at Re=170. The vibration frequency calculated on the cantilever due to vortex shedding from the bluff body is a constant everywhere at different Reynolds numbers (see Chapter 3, section 3.2), confirming that the motion is dominated by the first mode alone. At Re=170 to Re= 220, the frequency of vortex shedding from the bluff body is a constant; this is where the frequencies of the cantilever-alone and bluff body-alone match and hence lock-in. Figures 4-10 through 4-15 show ratios of vortex shedding frequency and natural frequency plotted against reduced velocity for different L/D ratios. The natural frequency is considered to correspond to the fundamental mode of vibration with respect to the length of the beam (see chapter 3). The frequency of vortex shedding is calculated from the lift force on different bluff-body sections. In the reduced velocity x-axis, the frequency is considered to be the natural frequency of the beam. Figures 4-16 through 4-21 show vorticity plots and streamline plots for different bluff bodies investigated at a particular L/D ratio and also for the configuration while it's locked-in and locked-out. Figure 4-22 shows the cylindrical bluff body with different L/D ratios at Re=180 which is inside the lock-in bandwidth for cylindrical bluff bodies.

For L/D=1.6, the cantilever beam for the cylindrical bluff-body locks-in at a lower Reynolds number flow range compared to the other two shapes, but fails to have a wide range of synchronization. The D-shaped bluff-body cantilever beams show a wider lock-in bandwidth for the higher Reynolds number flow regime. This is due to the larger shear forces over the bluff-bodies compared to the cylindrical bluff-body. The vortex pairs formed by vortex shedding shed a larger shear while the flow passes over the D-shaped bluff-body than the cylindrical bluff body. For Re=185-200, the cylindrical bluff body shows lock-in effect whereas D-shaped bluff body shows lock-in at Re=180-225. The pentagonal bluff-body locks-in for a small range and it shows an increase in f_s/f_n afterwards. The Strouhal number increases while the bluff-body is locked-in for a small range (Re=165-185). This is mainly due to the fact that the shear force developed from the bluff-body is not large enough to sustain the continuous formation of periodic vortex forces acting on the cantilever beam. The aerodynamic shape of the bluff-body is the reason behind this activity.

For L/D=1.7, the cantilever beam for the cylindrical bluff-body jumps from the lock-in region to a higher f_s/f_n ratio from Re=205 onwards. Hence this bluff-body model shows a narrow lock-in bandwidth. The jump is due to the low flow separation over the cylindrical bluff-body. For a D-shaped bluff-body model, the cantilever beam starts resonating at Re=190 until Re=240. The highest amplitude with a wider synchronous region is found due to the well formed vortices at the wake. Resonance occurs at Re= 197 for the pentagonal bluff-body cantilever beam model. The lock-in bandwidths for

pentagonal and cylindrical bluff-body shapes are comparable but have a lower bandwidth compared to the D-shaped bluff-body.

For L/D=1.8, the D-shaped bluff-body model cantilever beam resonates at the widest range of frequencies. The pentagonal bluff-body shows a lock-in region at low reduced velocities but shows a jump in frequency of vortex shedding afterwards. The cylindrical bluff-body shows a comparable physical phenomenon with the D-shaped bluff-body until a certain Reynolds number (Re=210) and loses synchronicity afterwards. Due to longer cantilever beam length, all the bluff-body models have a more aerodynamic construction. Consequently, the cantilever beam is not affected significantly by the shear forces acting on the bluff-body. The magnified versions of the lock-in regions for L/D=1.6, 1.7 and 1.8 are plotted in Figures 4-13 through 4-15.

Figures 4-16 through 4-21 show the different bluff bodies with the cantilever attached at lock-in and de-synchronized bandwidth. At lock-in, the cantilever beam oscillates or vibrates at the same frequency as the undisturbed wake behind the bluff-body (see Chapter 2). Figure 4-22 shows the cylindrical bluff body with different L/D ratios. For larger L/D ratios, the shape becomes an aerodynamic shape and hence, the wake vortex force from the bluff body is not strong enough to impinge the cantilever beam. The vortices take the form of the aerodynamic shape. For smaller L/D ratios, the cantilever beam is too short that the undisturbed wake will not strain the beam fully.

The next sets of results are the efficiency values of fluid to structural and structural to electrical power. This will help to validate if the lock-in range results are in par with the efficiency rates.

4.2.3 Transduction efficiency of the model

Simulation results for the energy efficiency of the model are investigated in this section. Energy efficiency calculated is the ratio of electrical power to mechanical power. Electrical power is calculated from Eq. 3.8 and simulated through a MATLAB code given in the Appendix. The transient simulations are run for 0 to 20 seconds of the flow. Mechanical power of the system calculated is simulated through COMSOL multiphysics software:

$$P_{Mech} = \int (\sigma \cdot u) dA \tag{4.7}$$

which is a line integration of the product of the stresses acting on the cantilever beam due to the normal component of the fluid pressure and velocity field in the z - direction. The power from the fluid is calculated from the basic principle of estimating fluid power through a wind turbine. The equation for which is:

$$P_{Fluid} = \tfrac{1}{2} \rho A u^3 \tag{4.8}$$

where $A = Db$ (b is the width of the bluff-body, b=10e-3). The area is taken as the frontal area of the bluff body. This concept is taken directly from the configuration of wind turbines [29]. Hence the efficiency of the power conversion from flow power to the mechanical power is:

$$\eta_{fm} = \frac{P_{Mech}}{P_{Fluid}} \tag{4.9}$$

The efficiency of mechanical power to electrical power is given by:

$$\eta_{me} = \frac{P_{Elec}}{P_{Mech}} \tag{4.9}$$

Subsequently, the total efficiency of the system is the product of efficiency of fluid power to structural power and structural power to electric power.

$$\eta_{total} = \eta_{fm}\eta_{me} \tag{4.10}$$

Simulations were done for Reynolds number ranging from Re=120 to Re=250 (see Figures 4-23 through 4-28). The x -axis is time and nondimensionalized by multiplying it with the natural frequency of the beam [30].

The cylindrical bluff-body shape shows a lock-in effect at a lower Reynolds number regime. For a cylinder at Re=121, the electrical power gain is higher for L/D=1.7 and L/D=1.8. Hence the efficiency is greater than the L/D=1.6 case. This outcome is due to smaller flow separation in the low Reynolds number regime for a cylindrical bluff-body. For Re=181, the efficiency of all L/D ratios of the cylindrical bluff-body model have a sudden increase due to the wider bandwidth of lock-in effect result discussed in the previous section. A sudden increase in the efficiency of Re=180 compared to Re=120 is

due to larger strain on the cantilever due to larger shear force from the bluff body. At Re=180, when L/D=1.8, the cylindrical model shows higher efficiency. Fluid pressure acting on the cantilever beam is larger due to the vortex geometry shearing off of the bluff-body. For the cylindrical bluff body, the maximum power gain is at two diameters away from the bluff-body.

For a D-shaped bluff-body configuration, at Re=180, maximum power gain occurs when L/D=1.6. But the cantilever beam locks-in for a wide range of Reynolds number flow regime, Re=180 to Re=250. At Re=200, maximum efficiency occur when L/D=1.7. The slight aerodynamic shape of the D-shaped bluff-body apparently gives it a combination of wider lock-in bandwidth and larger efficiency, unlike the pentagonal shape.

The pentagonal shape is more aerodynamic in nature than the D-shaped bluff-body, hence the flow separation is smaller and shear forces acting on the bluff-body are comparably low. The efficiency is comparable to the D-shaped bluff-body except when L/D=1.7 and Re=200. Also, the synchronous region for the pentagonal bluff-body is narrower when compared with the D-shaped bluff-body due to the aerodynamic shape. For L/D=1.8 and Re=200, maximum efficiency occurs.

The results show that D-shaped bluff-body model has the widest range of lock-in bandwidth and the maximum efficiency of the system when the cylindrical bluff-body model is at L/D=1.8 and Re=180.

These simulations and analysis are conducted so that a prototype for ambient testing and wind tunnel testing can be optimized by looking at two major factors, the L/D ratios of

the bluff-body cantilever beam model and also the velocity range at which maximum power gain and efficiency occur. Table 5 shows the concluding average electric power for the models tested. The cantilever beams that are locked-in have higher efficiency due to larger amplitude of oscillation for a longer time period.

Table 6 shows the concluding efficiencies of fluid power to mechanical power and mechanical power to electric power.

Table 3-Fluid property varying parameters

Varying Parameters		**Range**
Reynolds numbers	Re	50-2000
Bluff-body dimensions	*D*	0.001m-0.003m
Length of the cantilever beam	*L*	0.02m-0.04m
Thickness of the beam	*T*	0.0005m-0.001m

Table 4-Fluid property range and values

Fluid Properties		
Velocity	u	(0.01-3) m/s
Density	ρ	1.2 kg/m^3
Dynamic Viscosity	μ	1.985e-005 $Pa*s$

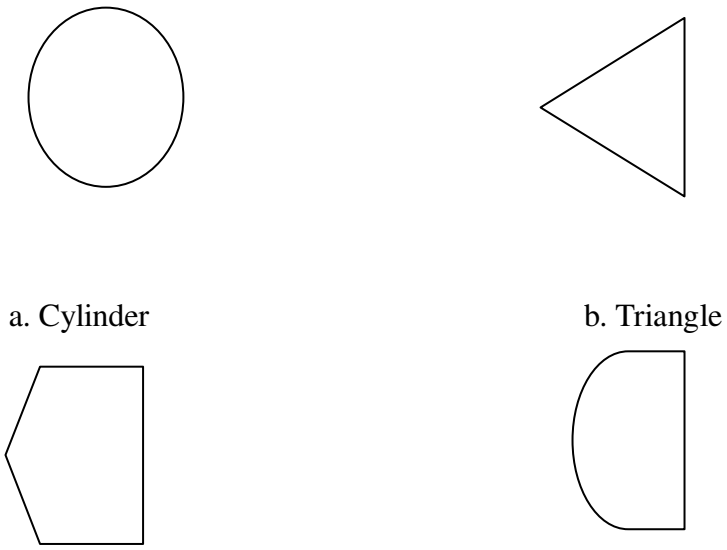

Figure 4-1- Bluff Bodies Investigated

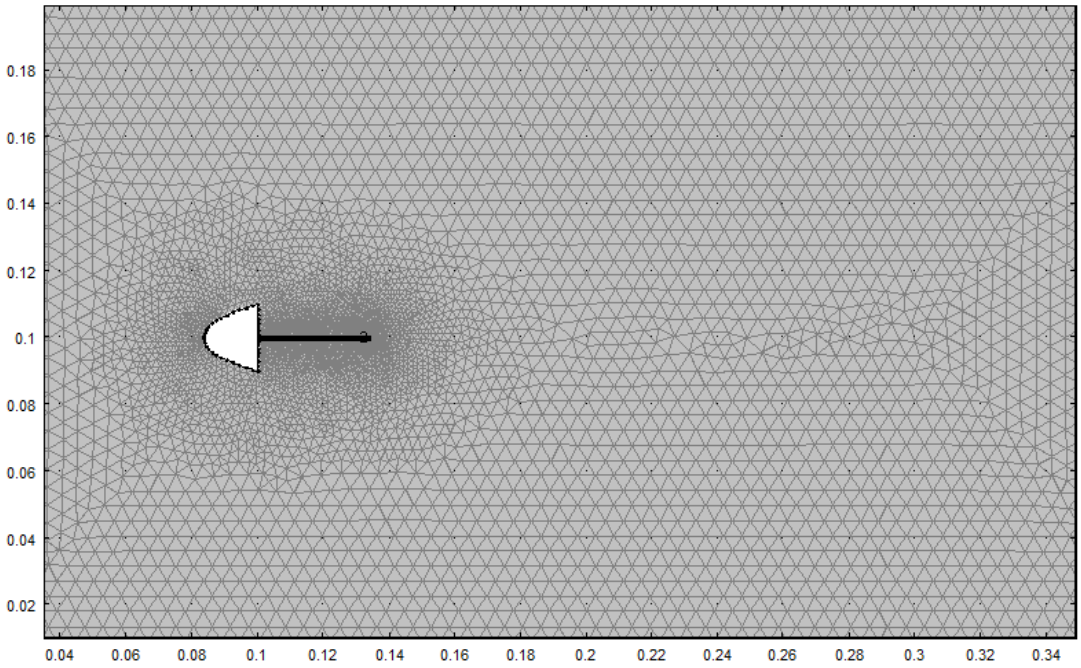

Figure 4-2- Representation of triangular mesh with D-Shaped as the bluff body and the cantilever beam

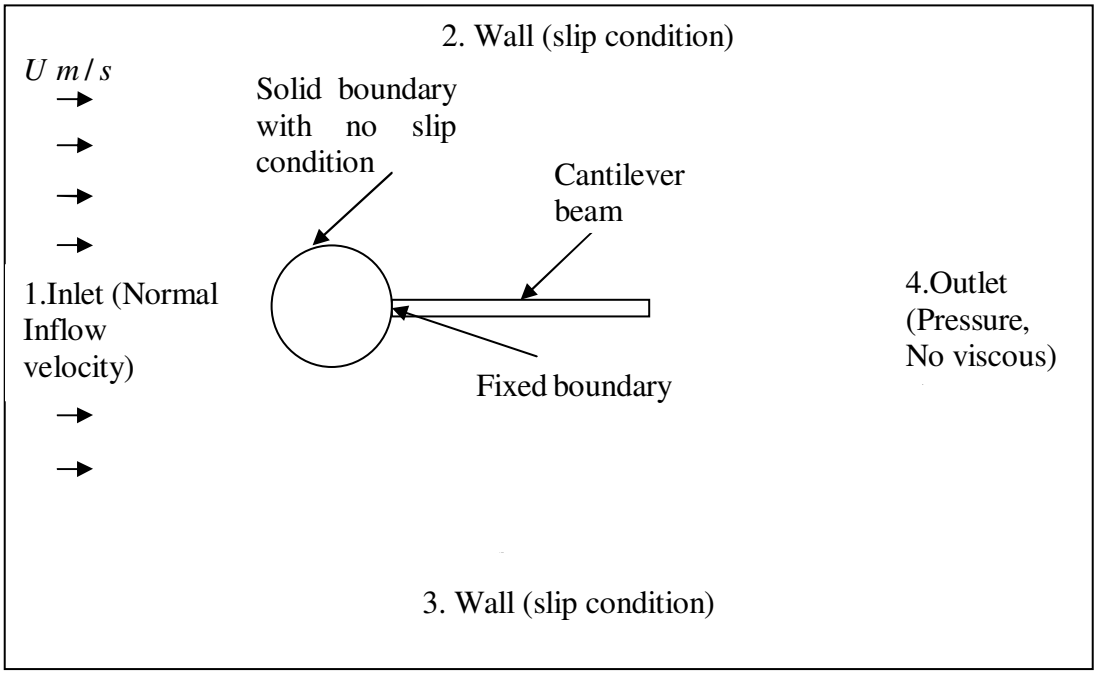

Figure 4-3- Diagrammatic representation of boundary conditions used in the CFD simulations

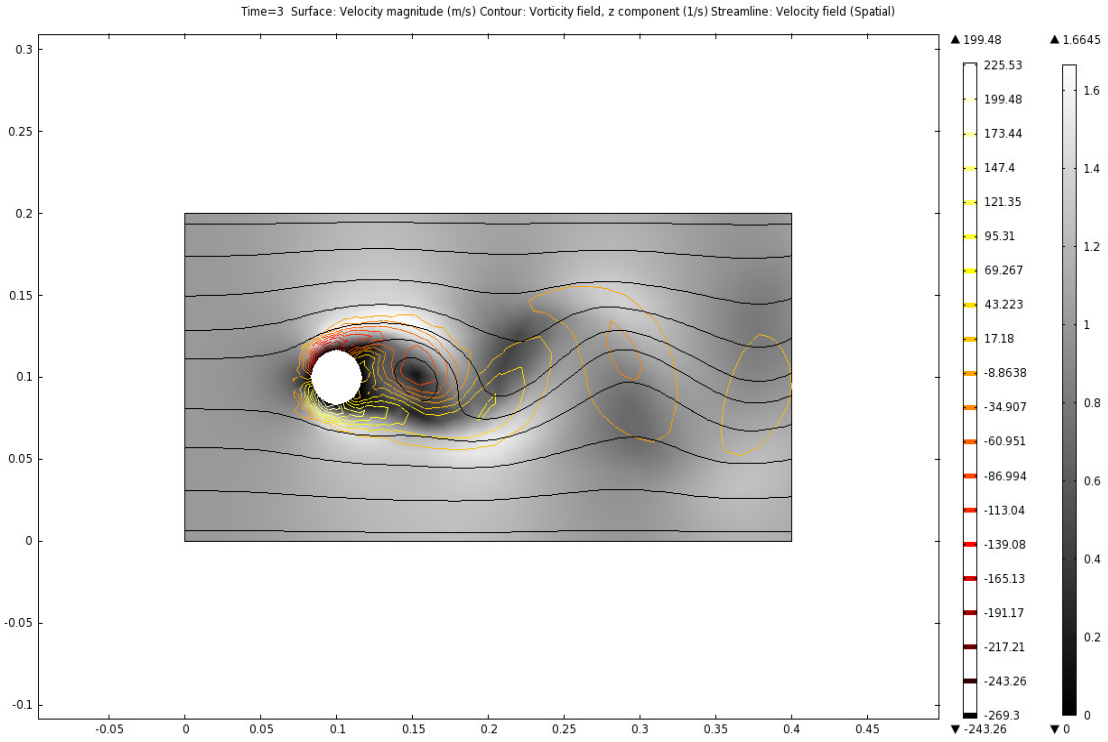

Figure 4-4- Velocity and Vorticity contour plots for a cylindrical bluff-body (Re=1200)

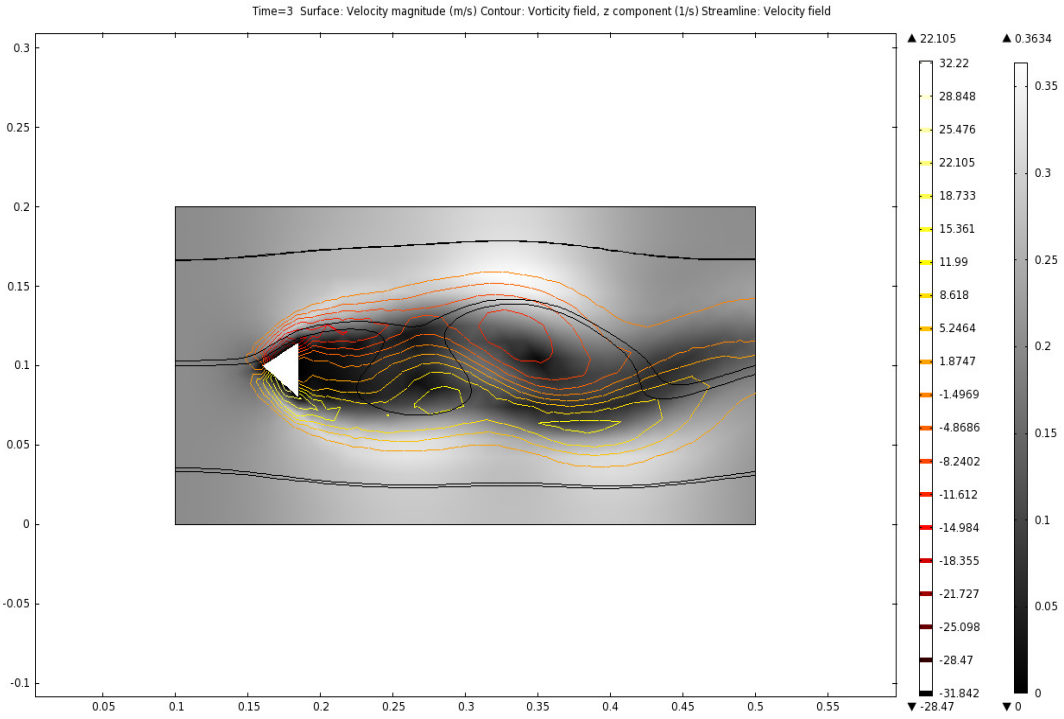

Figure 4-5- Velocity and Vorticity contour plots for a Triangular bluff-body (Re=1200)

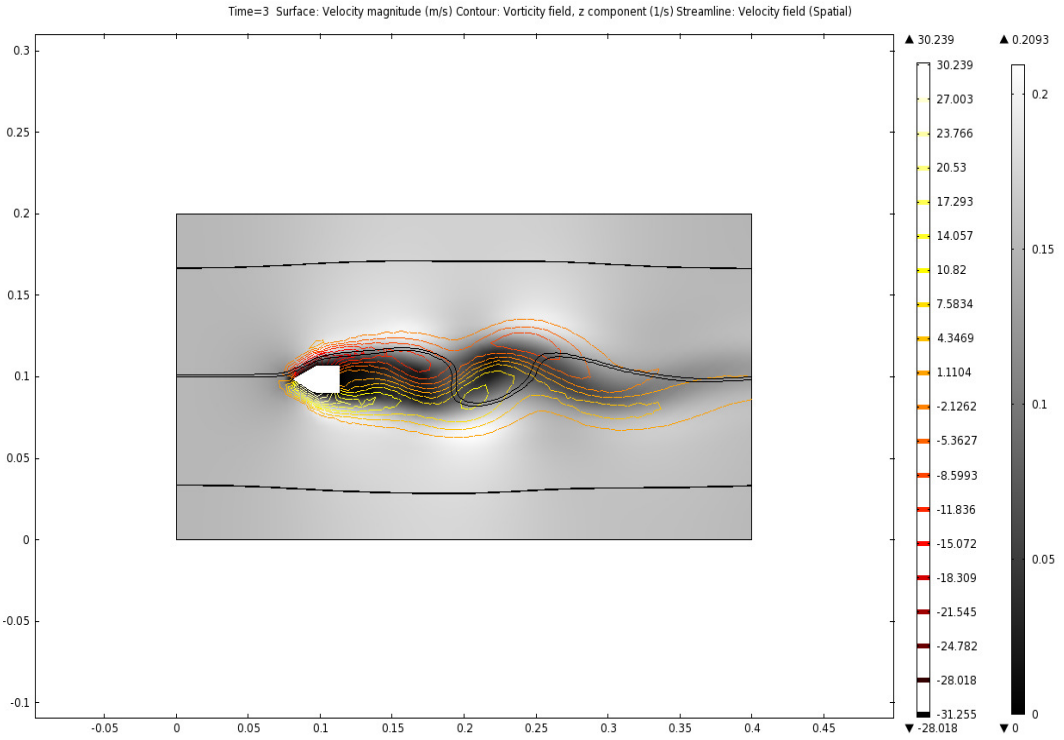

Figure 4-6- Velocity and Vorticity contour plots for a pentagonal bluff-body (Re=1200)

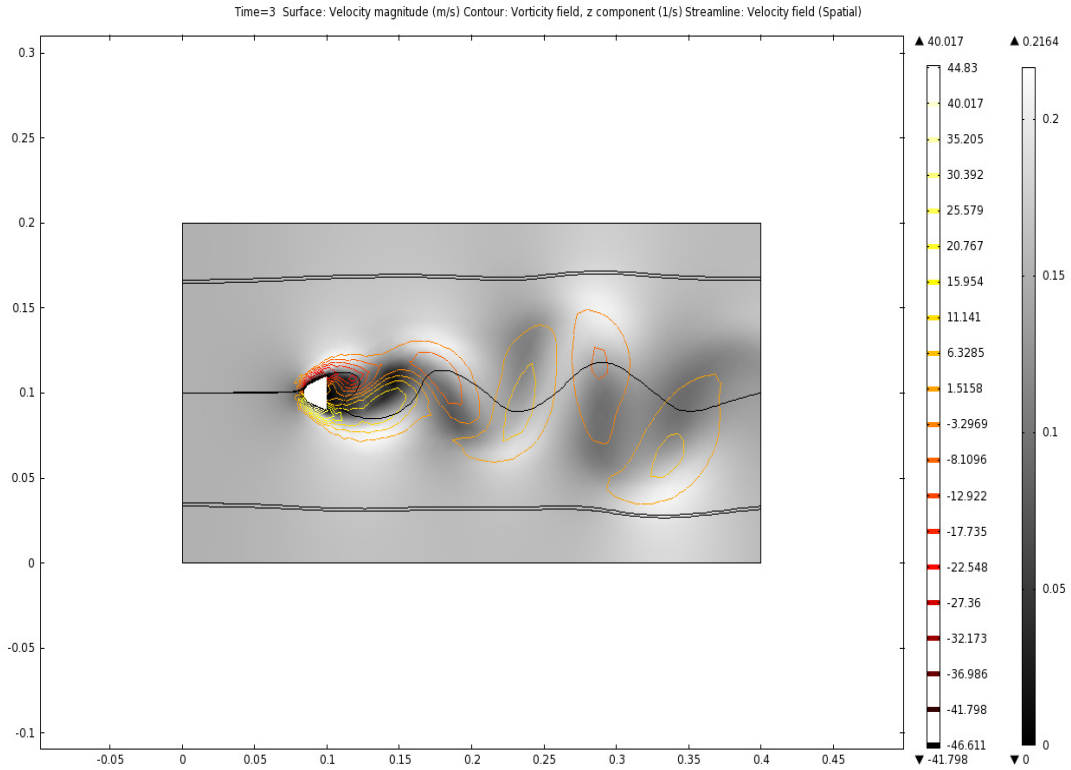

Figure 4-7- Velocity and Vorticity contour plots for a D-shaped bluff-body (Re=1200)

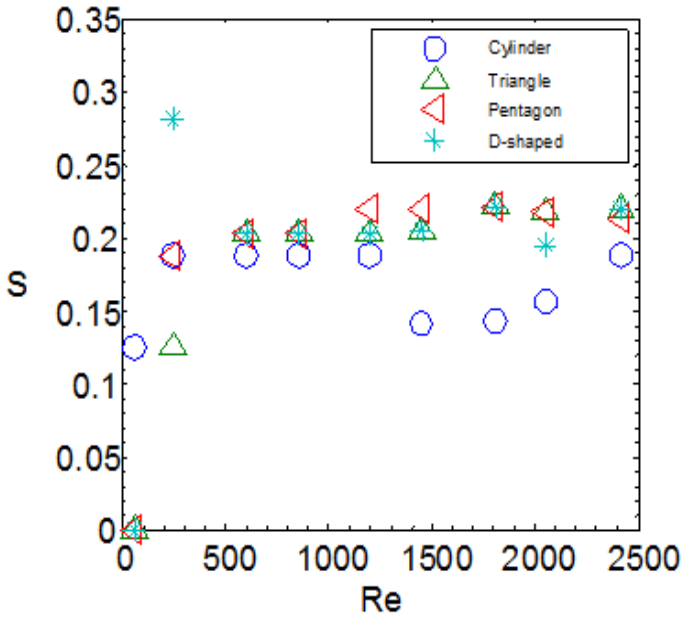

Figure 4-8- Strouhal Number Vs Reynolds number for different bluff-body shapes

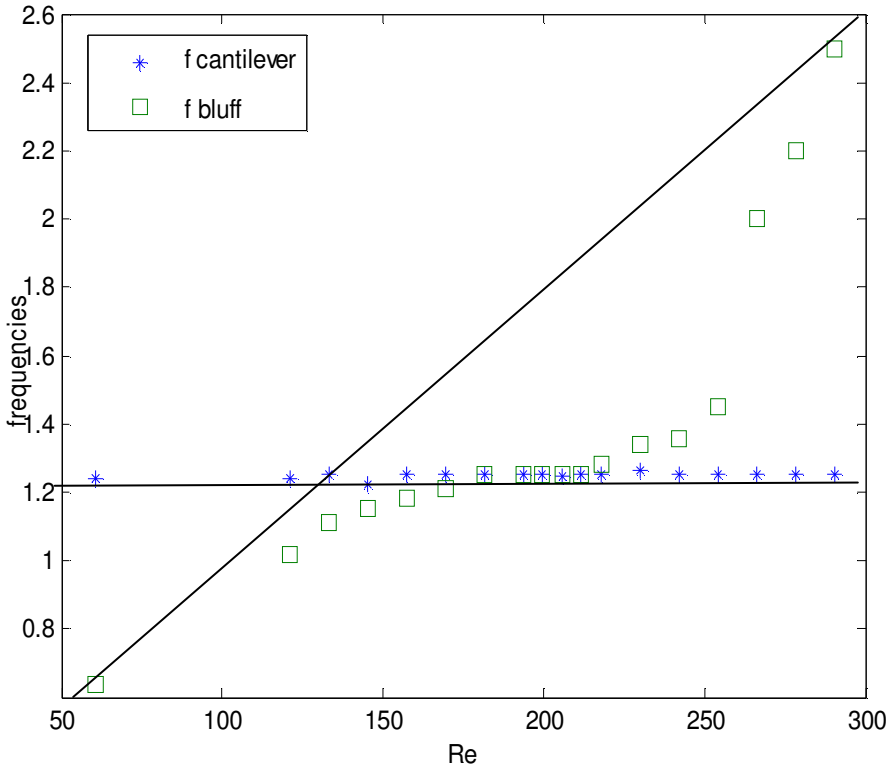

Figure 4-9- Reynolds number Vs Frequencies of cantilever-alone and bluff body-alone for cylindrical bluff body

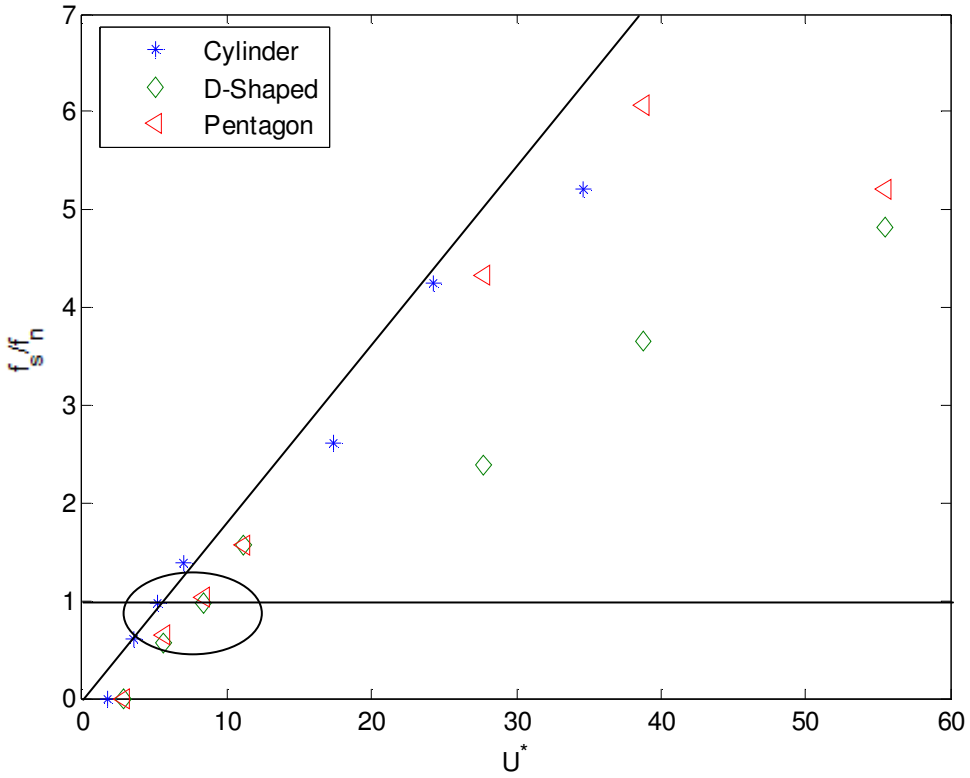

Figure 4-10- L/D ratio = 1.6

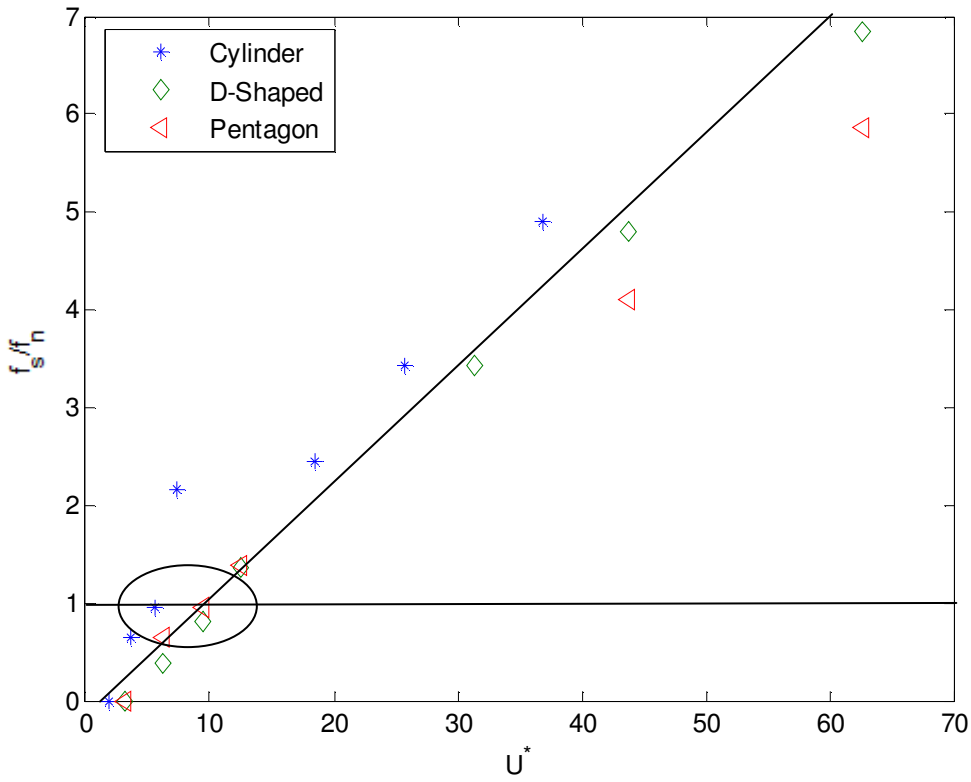

Figure 4-11- L/D ratio = 1.7

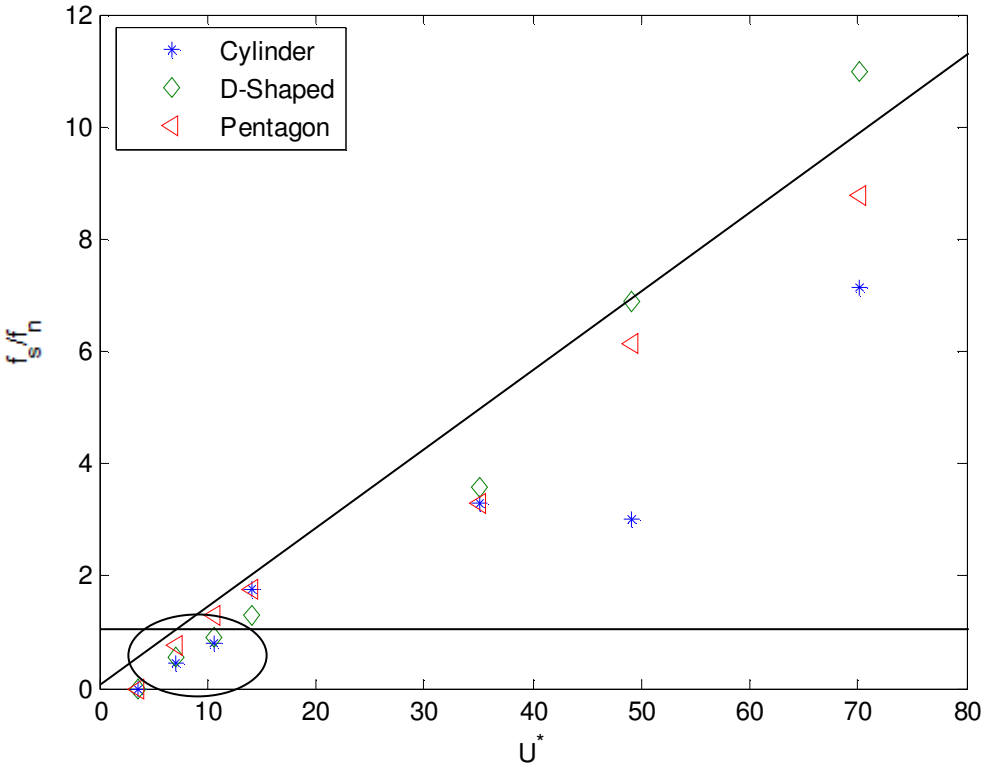

Figure 4-12- L/D ratio = 1.8

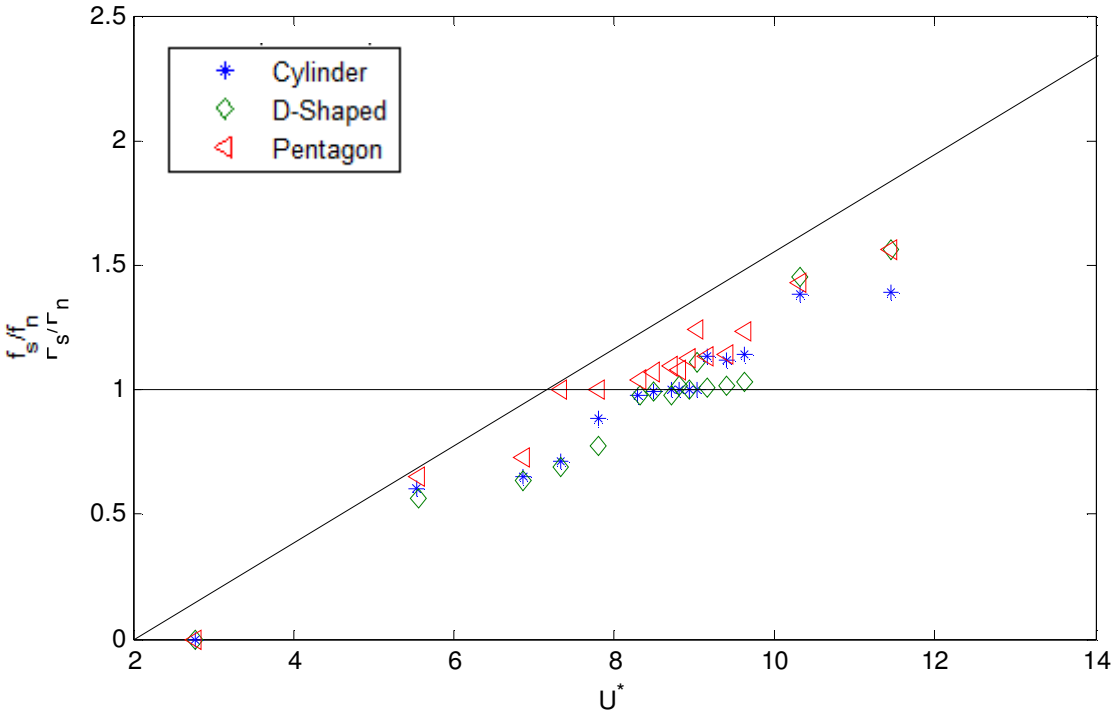

Figure 4-13- Magnified version of L/D ratio = 1.6

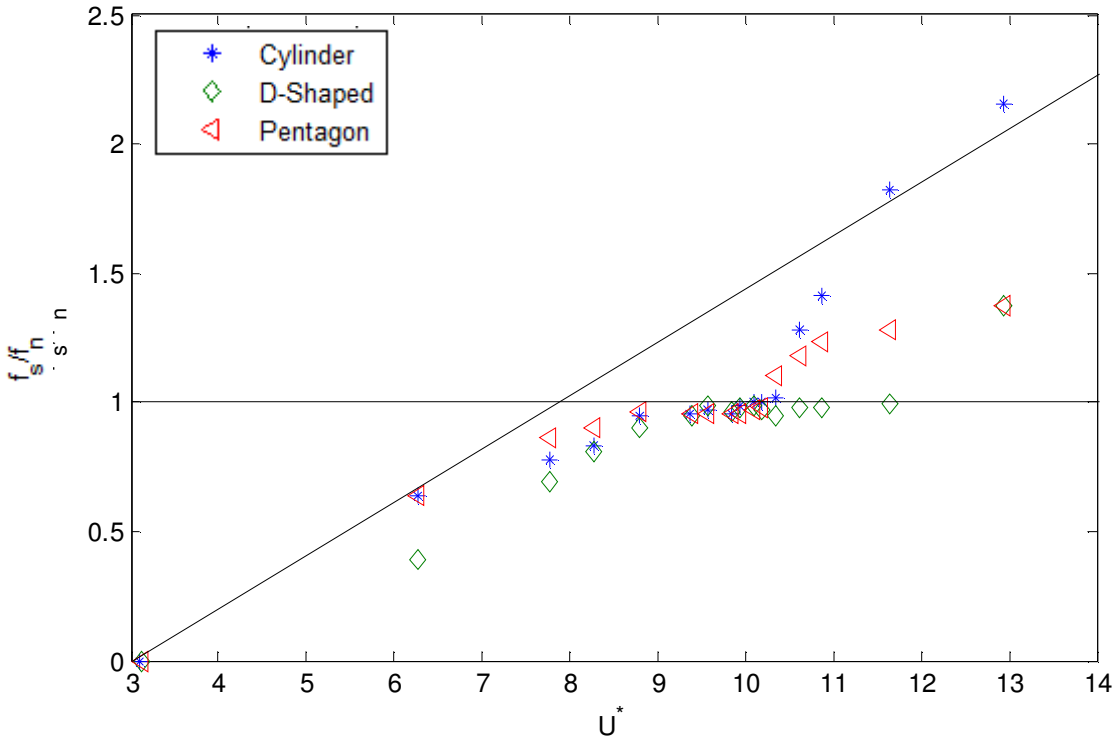

Figure 4-14- Magnified version of L/D ratio = 1.7

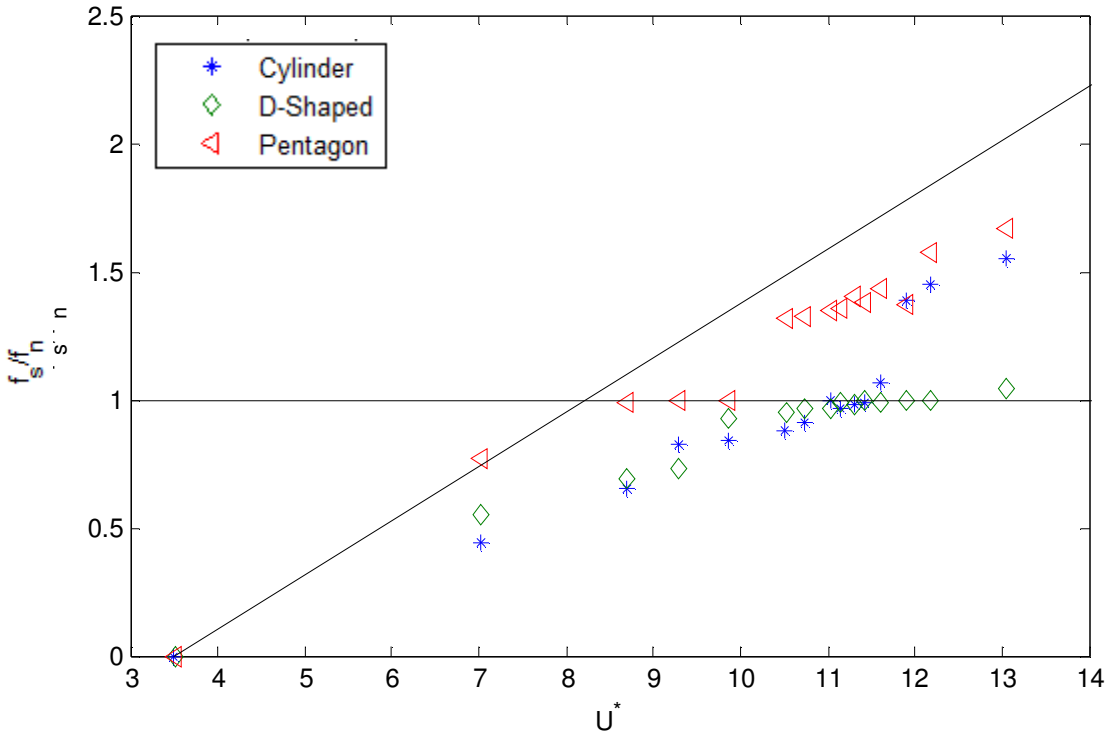

Figure 4-15- Magnified version of L/D ratio = 1.8

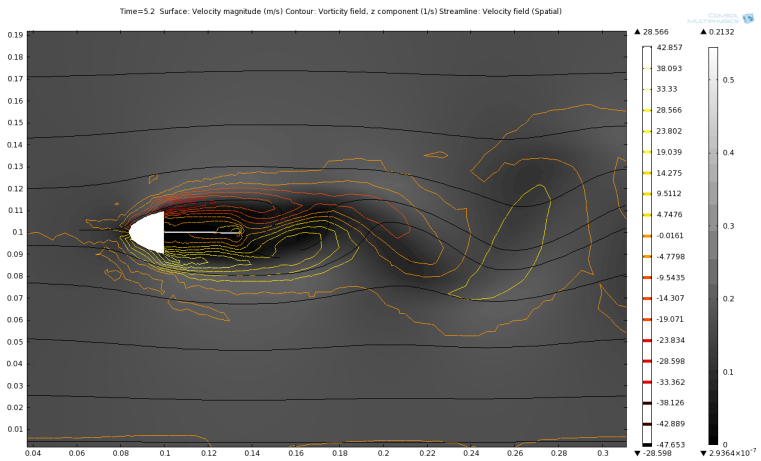

Figure 4-16- D-shaped locked-in Re=195, L/D=1.7

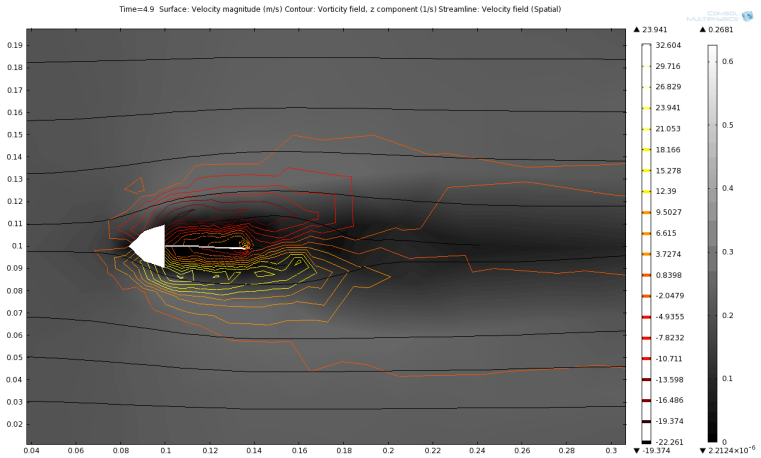

Figure 4-17- D-shaped de-synchronized Re=250, L/D=1.7

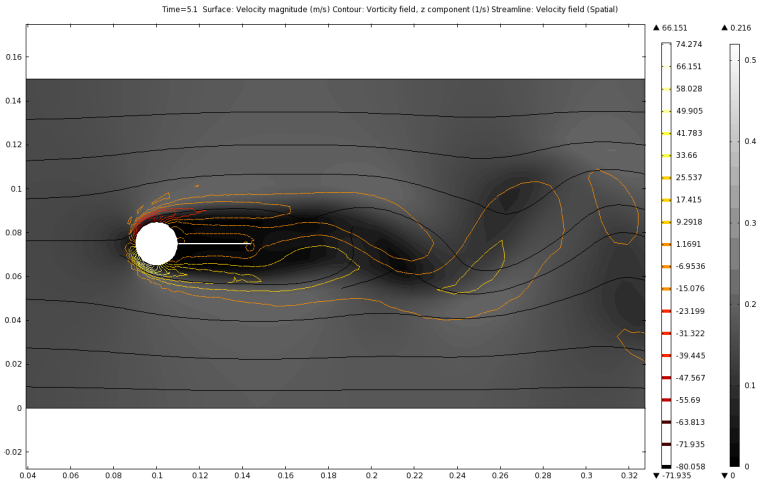

Figure 4-18- Cylinder locked-in Re=181, L/D=1.7

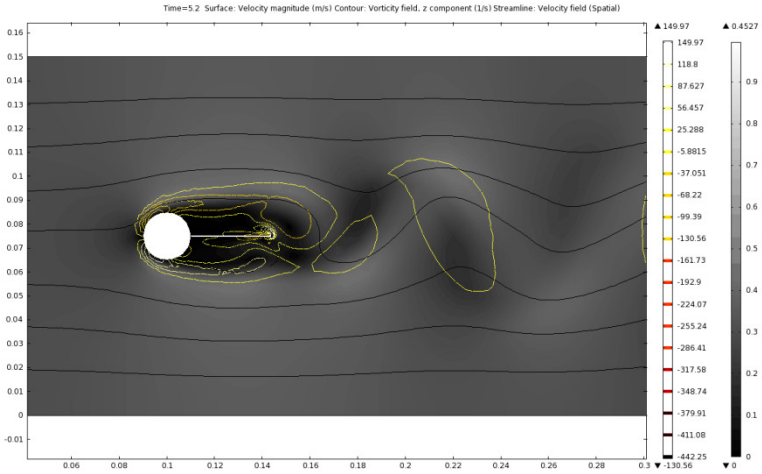

Figure 4-19- Cylinder de-synchronized Re=240, L/D=1.7

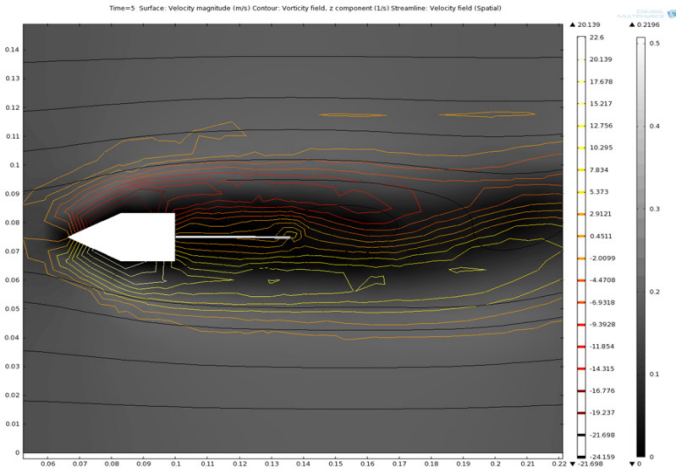

Figure 4-20- Pentagon locked-in Re=180, L/D ratio = 1.7

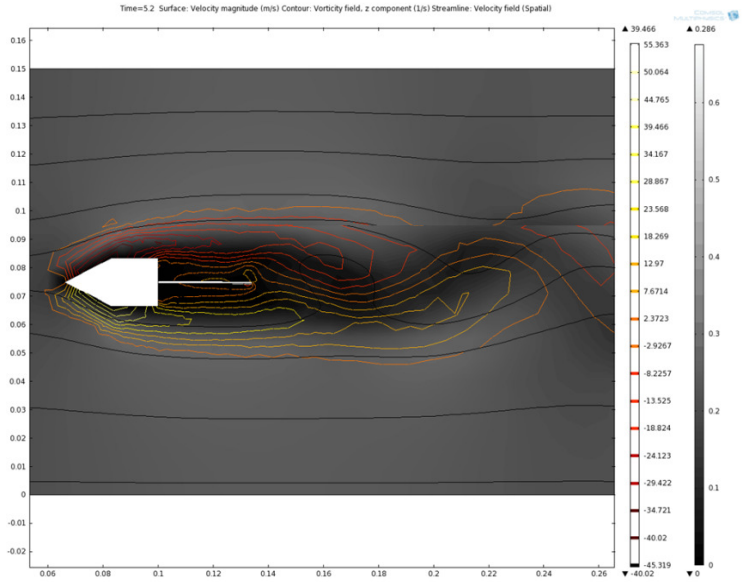

Figure 4-21- Pentagon de-synchronized Re=200, L/D ratio = 1.7

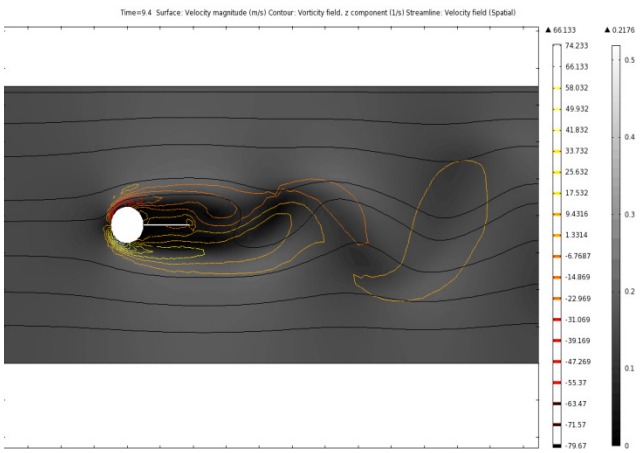

L/D=1.4

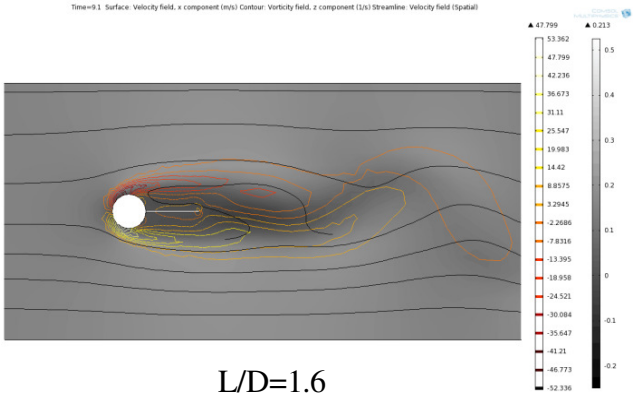

L/D=1.6

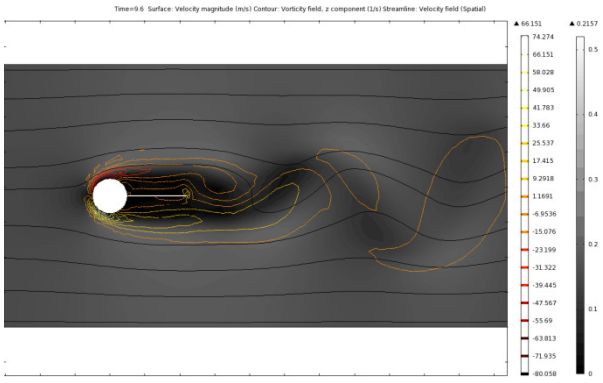

L/D=1.7

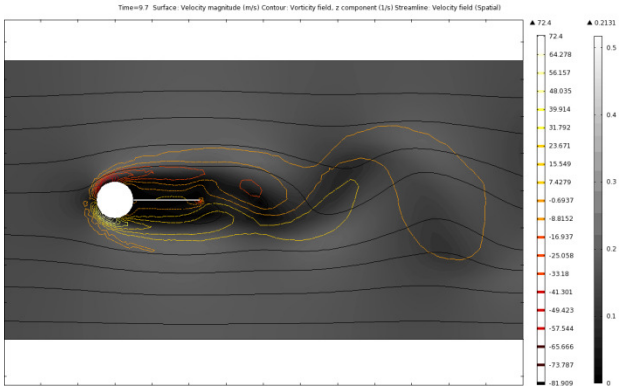

L/D=1.8

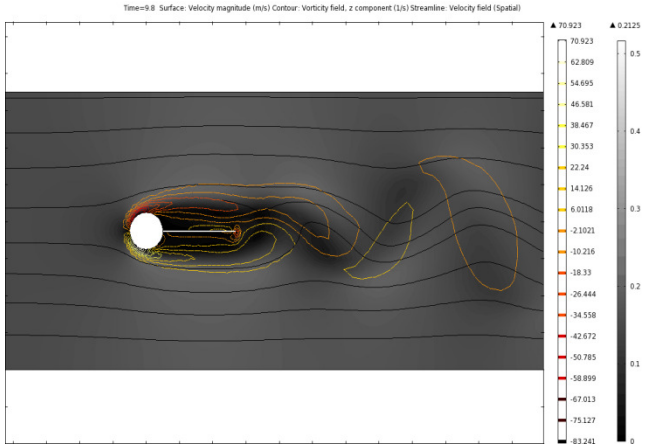

L/D=2.2

Figure 4-22- Cylinder with different L/D ratios, Re=180

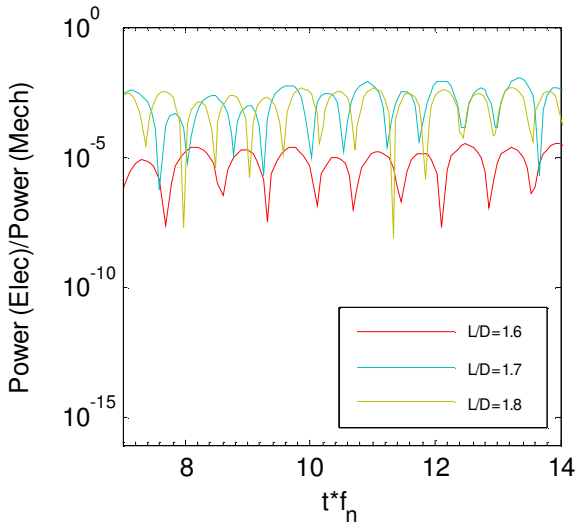

Figure 4-23- Energy efficiency of a cylindrical bluff-body model Re=121

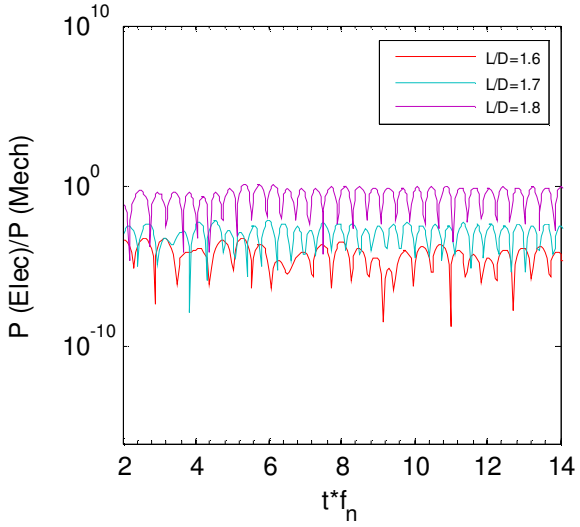

Figure 4-24- Energy efficiency of a cylindrical bluff-body model Re=180

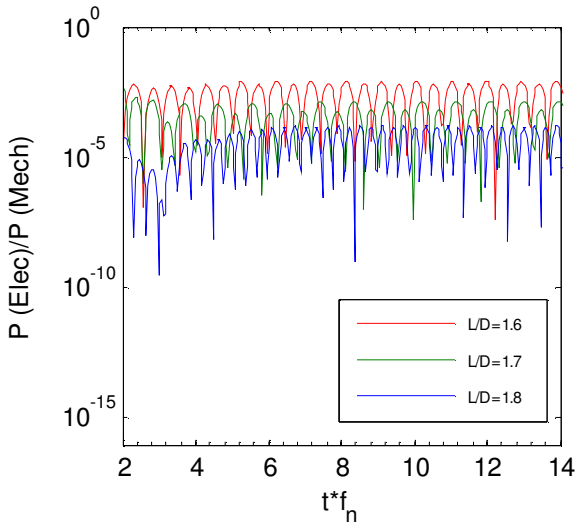

Figure 4-25- Energy efficiency of a D-shaped bluff-body model Re=180

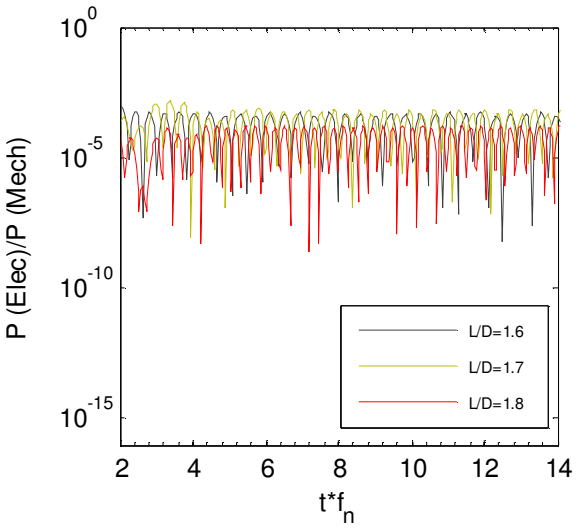

Figure 4-26- Energy efficiency of a D-shaped bluff-body model Re=200

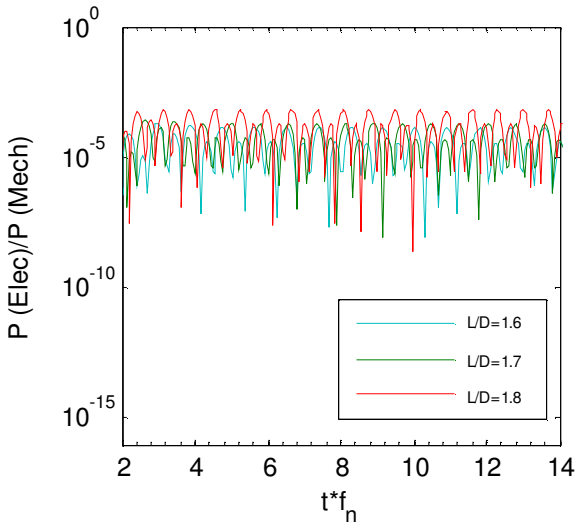

Figure 4-27- Energy efficiency of a pentagonal bluff-body model Re=180

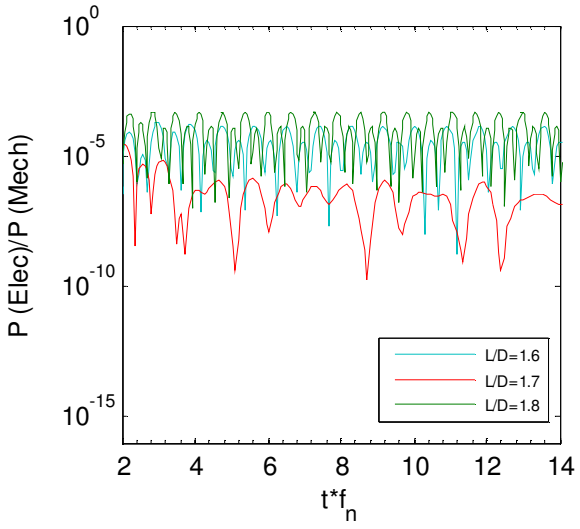

Figure 4-28- Energy efficiency of a pentagonal bluff-body model Re=200

Table 5-Average electric power for different bluff-bodies

Bluff-body shape	Reynolds number	Average power (μW)
Cylinder	120-250	0.20
D-Shaped	120-250	0.22
Pentagon	120-250	0.15

Table 6-Average power efficiencies for different bluff-bodies at

L/D ratio =1.7

Bluff-body shape	Reynolds number	η_{fs}	η_{se}	η_{total}
Cylinder	120-250	0.029	0.10	0.0029
D-Shaped	120-250	0.031	0.12	0.00372
Pentagon	120-250	0.022	0.09	0.00198

Conclusion

A small-scale energy harvesting technique using vortex induced vibrations (VIV) and bluff-body vibrations is studied. Driving oscillating forces generated from the bluff-body induced by the von Kármán vortex streets mechanically strain piezoelectric cantilever beams attached to the bluff-body, and power is generated. Extensive studies of dimensionless parameters – Strouhal number, Reynolds number, reduced velocity, ratio of vortex shedding frequency to natural frequency, dimensionless power, and dimensionless time – on four different bluff-body sections – namely cylindrical, triangular, pentagonal, and D-shaped bluff bodies – are studied. The first chapter introduces the historic relevance of VIV, a literature review about different VIV techniques, and how the destructive nature of VIV can be used to harness energy through piezoelectric transduction. The mathematical and physical basis of the complicated fluid structure interaction modeling is presented. The physics is based on the Arbitrary Lagrangian Eulerian moving mesh method. Afterwards, the electromechanical modeling is presented, where a distributed-parametric dynamic equation is derived by coupling the Euler-Bernoulli cantilever beam theory and the linearized equations for piezoelectric equations. The concluding chapter presents simulations and results for the model from COMSOL Multiphysics and MATLAB simulations. The thesis problem is validated by taking into account the physical modeling, the mathematic modeling and simulations, and proves that maximum energy is extracted when the cantilever beams resonate at the highest amplitude with the frequency of vortex shedding and hence within the lock-in band. The most optimized harvester design in terms of efficiency and over a wide-range of lock-in from this study is concluded to be the design

with the D-shaped bluff body. The average total efficiency of the D-shaped bluff body between the lock-in bandwidth is found to be 0.00372.

Future Work

The present configuration is a bluff body with a flexible piezoelectric cantilever attached to the trailing edge. Another configuration which consists of a flexible vertical cantilever clamped at the base with a bluff body tip mass can be designed and validated in the future. A novel design, which combines the first two configurations, can be a possible future work. This novel idea consists of a flexible vertical cantilever design attached to the bluff body configuration. Investigating the combined power gain can be a possibility. Also, to validate the thesis design experimentally, turbulent and laminar wind tunnel experiments using a non-steady generator generating wind gusts can be a possible project in the future.

References

[1] Blevins, R., D. (1994). *Flow-induced vibrations* (second ed.). Malabar, Florida: Krieger Publishing Company.

[2] Elizabeth., G., M. (2008). Prediction by energy phenomenology for harnessing hydrokinetic energy using vortex-induced vibrations. (Doctor of Philosophy, The University of Michigan).

[3] Hall, S., A. (1981). Vortex-induced vibrations of structures. (Doctor of Philosphy, California Institute of Technology).

[4] Strouhal, V. (1878). Ueber eine besondere art der tonerregung. *Ann. Physik (Leipzig).*

[5] Rayleigh, J. W. S. (1945). *The theory of sound vol. II* (Second Ed. ed.). N. Y.: Dover Publication.

[6] Bearmen, P. (1984). Vortex shedding from oscillating bluff bodies. *Annual Review of Fluid Mechanics, 16*(1), 195.

[7] Williamson., C. H. K. and Govardhan., R. (2004). Vortex-induced vibrations. *Annual Review of Fluid Mechanics, 36*, 415-455.

[8] Bernistat, M. M., Raghavan, K., Ben-imon, Y., and Garcia, E. M. H. (2008). VIVACE(vortex incuced vibration acquatic clean energy): A new concept in generation of clean and renewable energy from fluid flow. *Journal of Offshore Mechanics and Arctic Engineering Transaction of the Asme, 130*(4).

[9] Parkinson, G., V., Feng, C., C. and Ferguson, N. (1968). Mechanisms of vortex-excited oscillation of bluff cylinders. *Loughborough Univ of Technology.*

[10] Erturk, A., Vieira, W.G.R., De Marqui, C. Jr. and Inman, D.J. (2010). On the energy harvesting potential of piezoaeroelastic systems. *Applied Physics Letter, 96*(18), 184103-184105.

[11] Jung, Hyung-Jo., Lee, Seung-Woo. and Jang, Dong-Doo. (2009). Feasibility study on a new energy harvesting electromagnetic device using aerodynamic instability. *IEEE Trans. Magn., 45*(10), 4376-4379.

[12] Priya, S. and Inman, D.J. (2009). *Energy harvesting technologies* (1st ed.). New York: Springer Science+Business Media.

[13] Allen, J., J. and Smits, A., J. (2001). Energy harvesting EEL. *Journal of Fluids and Structures, 15*, 629-640.

[14] Bischur, E., Pobering, S., Menacher, M. and Schwesinger, N. (2010). Piezoelectric energy harvester operating in flowing water. *Proceeding of SPIE,* San Diego. (7643) 76432Z-1.

[15] Pobering, S., Ebermeyer, S. and Schwesinger, N. (2009). Generation of electrical energy using short piezoelectric cantilevers in flowing media. San Diego. (7288) 728807.

[16] Akaydln, H.D., Elvin, N. and Andreopoulos, Y. (2010). Wake of a cylinder: A paradigm for energy harvesting with piezoelectric materials. *Experiments in Fluids, 19*(6), 065020.

[17] Li, Shuguang. and Lipson, Hod. (2009). Vertical-stalk flapping-leaf generator for wind energy harvesting. *Proceedings of ASME Conference for Smart Materials, Adaptive Structures and Intelligent Systems, , SMASIS2009* 611-619.

[18] Bryant, M. and Garcia, E. (2011). Modeling and testing of a novel aeroelastic flutter energy harvester. *Journal of Vibration, 133*(1), 011012-1-011012-11.

[19] Wickenheiser, A., M. and Garcia, E. (2010). Power optimization of vibration energy harvesters utilizing passive and active circuits. *Journal of Intelligent Materials Systems and Structure, 21*(13), 1343-1361.

[20] Shu, Y. C., Lien, I. C., and Wu, W. J. (2007). An improved analysis of the SSHI interface in piezoelectric energy harvesting. *Smart Materials and Structures, 16*, 2253-2264.

[21] Lefeuvre, E., Badel, A., Richard, C., and Guyomar, D. (2005). Piezoelectric energy harvesting device optimization by synchronous charge extraction. *Journal of Intelligent Material Systems and Structures, 16*, 865-876.

[22] Achenbach, E. and Heinecke, E. (1981). *On vortex shedding from smooth and rough cylinders in the range of reynolds number 6 multiplied by 10^3 to 5 multiplied by 10^6. Journal of Fluid Mechanics, 109*, 239-251.

[23] Lienhard, J., H. and Liu, L., W. (1967). Locked-in vortex shedding behind oscillating circular cylinders, with application to transmission lines. *American Society of Mechanical Engineers -- Papers, ASME FE-24,* New York. 67-FE-24.

[24] Roshko, A., (1955). Wake and drag of bluff bodies. Journal of Aeronautical Sciences, 22(n 2), 124-132

[25] Gerrard., J. H. (1966). The mechanics of the formation region of vortices behind bluff bodies. *Journal of Fluid Mechanics, 25*(02), 401-413.

[26] Comsol, AB., (2004). Femlab ALE models reference guide", http://www.comsol.com.

[27] Standards Committee of the IEEE Ultrasonics, Ferroelectrics, and Frequency Control Society, "IEEE standard on piezoelectricity," 54(1988).

[28] Sivadas, V. and Wickenheiser, A. M. (2011). A Study of Several Vortex-Induced Vibration Techniques for Piezoelectric Energy Harvesting," Proceedings of SPIE, Vol. 7977, March 6-10, San Diego, CA.

[29] Akaydin, H. D., Elvin, N. and Andreopoulos, Y. (2011). Energy harvesting from highly unsteady fluid flows using piezoelectric materials. *Journal of Intelligent Material Systems and Structures, 0*(13), 1263-1278.

[30] Sivadas, V. and Wickenheiser, A.M. (2011). Small-scale Wind Energy Harvesting from Flow-induced Vibrations", *ASME Conference on Smart Materials, Adaptive Structures and Intelligent Systems*, SMASIS2011-5106, September 18-21, Pheonix, AZ.

Appendix

MATLAB Script for Power and Voltage from Piezoelectric Transduction

```
clear all;
close all;

% beam geometry
L = 0.032;
% length (m)
b = 10e-3;
% width (m)
t_s = 0.8e-3;
% thickness of substrate (m)
t_p = 1.5e-3;
% thickness of PZT (m)
c_1_p = 66e9;
% 1-stiffness of PZT-5A (Pa)
d31 = -190e-12;
% piezoelectric constant (m/V)
e31 = d31*c_1_p;
eps33 = 15.93e-9;
% permittivity (F/m)

% effective beam parameters
C_0 = 2*eps33/t_p*b*L;
% net clamped capacitance (F)
tht = -e31*b*(t_p+t_s);
% piezo layers coupling coefficient (N-m/V)
R_L = 1/(C_0*4.59);
% load resistance (Ohm)

% data set
fname_cylinder = '181Re_Small_C.xlsx';
t_vec = 0:.1:20;
x_vec = [  0.115        0.12        0.125        0.13        0.135
0.14        0.142]';
w_data = xlsread([cd '\Cylinder\' fname_cylinder],'A3:G203');
% read in last 4 columns (to get good estimate of slope at tip)
% w_data = w_data - 1e-3;

% figure;
% plot(t_vec,w_data);

% figure;
% plot(x_vec,w_data);

wt_pp = pchip(t_vec,w_data');
% build w(t) pchip at each x
```

```
wx_pp = pchip(x_vec,w_data);
% build w(x) pchip at each t

xx_vec = linspace(0,L,101);
% figure;
% plot(xx_vec,ppval(wx_pp,xx_vec));

% tt_vec = 0:.01:5;
figure;
plot(t_vec,ppval(wt_pp,t_vec));

% compute dw/dx at x=L
[x,rho,~,~,d] = unmkpp(wx_pp);
% size(x)
% size(rho)
% size(L)
% size(k)
drho = [3*rho(:,1) 2*rho(:,2) rho(:,3)];
dwdx_pp = mkpp(x,drho,d);

% figure;
% plot(xx_vec,ppval(dwdx_pp,xx_vec));

dwdx_L = ppval(dwdx_pp,xx_vec(end));

% figure;
% plot(t_vec,dwdx_L);

% compute d2w/dxdt at x=L
dwdx_L_pp = pchip(t_vec,dwdx_L);

% figure;
% plot(tt_vec,ppval(dwdx_L_pp,tt_vec));

% simulate AC circuit dynamics to solve for v(t)
v0 = tht*R_L*ppval(dwdx_L_pp,0);
% initial voltage (V)
tspan = [t_vec(1) t_vec(end)];
[t,v] = ode45(@loc_ode_fun,tspan,v0);

function zdot = loc_ode_fun(this_t,z)

zdot = tht/C_0*ppval(dwdx_L_pp,this_t) - z/(R_L*C_0);

end

figure;
plot(t,v);
ylabel('Voltage, V');
xlabel('Time, s');
Mech_cylinder = '181Re_Large_C_Mech.xlsx';
```

```
Mech_Power = xlsread([cd '\Cylinder\' Mech_cylinder],'o3:o203');
%Read Mechanical power

figure;
plot(t*0.9112,v.^2/R_L);
ylabel('Power, W');
xlabel('Time, s');

figure;
plot(t*0.9112,(v.^2/R_L)/Mech_Power);
ylabel('ElecPower/MechPower');
xlabel('Time*Fn');
M=mean2((v.^2/R_L)/Mech_Power)

end
```

MATLAB Script for Calculating Strouhal Number

```
clc;
clear all;
close all;
t_vec = (0:0.01:2);
U=0.05; %Flow speed

% Read values from spreadsheet
St= '\Strouhal number FFT_data.xlsx';
t_vec = xlsread([cd St],'C4:C204');
lift_vec = xlsread([cd St ],'D4:D204');


figure;
plot(t_vec,lift_vec); %Shedding frequency Vs Time

% start fft calculation at t = 20s
ind = t_vec>.5*t_vec(end);
t_vec = t_vec(ind);
lift_vec = lift_vec(ind);
c=mean(lift_vec)
%FFT Analysis
NFFT = 2^nextpow2(length(lift_vec)); % Next power of 2 from length
of y
Y = fft(lift_vec,NFFT)/length(lift_vec);
f = 1/(t_vec(2)-t_vec(1))/2*linspace(0,1,NFFT/2+1);
% Y=abs(fft(vec)); %FFT
figure
stem(f,2*abs(Y(1:NFFT/2+1)))
figure
plot(f,2*abs(Y(1:NFFT/2+1)))
[m,ind] = max(abs(Y));
f_s = f(ind);
str=(f_s*.02)/U
```